

Entanglement dynamics in the many-body Hatano-Nelson model

Takahiro Orito

Graduate School of Advanced Science and Engineering, Hiroshima University, 739-8530, Japan
Institute for Solid State Physics, The University of Tokyo 5-1-5 Kashiwanoha, Kashiwa 277-8581, Japan

Ken-Ichiro Imura

Institute of Industrial Science, The University of Tokyo 5-1-5 Kashiwanoha, Kashiwa 277-8574, Japan

(Dated: August 8, 2023)

The entanglement dynamics in a non-Hermitian quantum system is studied numerically and analyzed from the viewpoint of quasiparticle picture. As a concrete model, we consider a one-dimensional tight-binding model with asymmetric hopping (Hatano-Nelson model) under onsite disorder and nearest-neighbor interaction. As opposed to an assertion of previous studies, the entanglement dynamics in this non-Hermitian quantum system is very different from the one in its Hermitian counterpart, especially in the delocalized regime with weak disorder; there the entanglement entropy $S_{\text{ent}}(t)$ shows a characteristic non-monotonic time evolution. We have clarified and quantified the nature of this behavior in the quasiparticle picture. In the asymptotic regime of $t \rightarrow \infty$, the entanglement entropy $S_{\text{ent}}(t)$ in this regime saturates to a much suppressed value, which increases only logarithmically with respect to the size of the subsystem.

I. INTRODUCTION

The entanglement entropy S_{ent} quantifies non-local correlation between quasiparticles in a many-body quantum state, such as the one in an EPR (Einstein-Podolsky-Rosen) pair.^{1–6} In the process of quantum thermalization^{7–9} or relaxation^{10–13}, the so-called quasiparticle picture^{14–18} (Fig. 1) makes this point explicit. A pair of entangled quasiparticles generated at $t = 0$ move apart, and as time passes by, they are more likely found in a different subsystem; see panel (a) of Fig. 1. This leads to an increase of the entanglement entropy S_{ent} ; cf. its bipartite definition, Eq. (17). Correspondingly, the reduced density matrix of the subsystem becomes a *mixed* state [cf. Eq. (18)].^{19,20}

In a system in which this quasiparticle picture is well applicable, the entanglement entropy S_{ent} is an extensive quantity, obeying the volume law²¹: $S_{\text{ent}} \propto V = L^d$ (L : size, d : dimension of the system); and indeed serves a *thermodynamic* quantity, while there are cases in which S_{ent} obeys the area law scaling $S_{\text{ent}} \propto V = L^{d-1}$. The latter includes the cases of non-unitary time evolution induced by dissipation,²² projective measurements,^{23,24} and also some parameter regime of a PT symmetric system.^{25,26} If one can manipulate a parameter of the system drive the system from one case to the other, the entanglement entropy S_{ent} is subject to a transition from volume to area law scaling.²³ This transition, dubbed as the entanglement transition, has been attracting much attention recently, in theoretical,^{27–33} experimental,^{34,35} and numerical contexts.^{36–38}

We consider, as a concrete example, the case of a many-body Hatano-Nelson (HN) model;^{39–41} a one-dimensional tight-binding model with asymmetric (non-reciprocal) hopping, the latter specified by a parameter g . In dynamics, due to the asymmetry in hopping, an initial wave packet does not spread as in the Hermitian case, but rather slides in the direction specified by the asymmetry

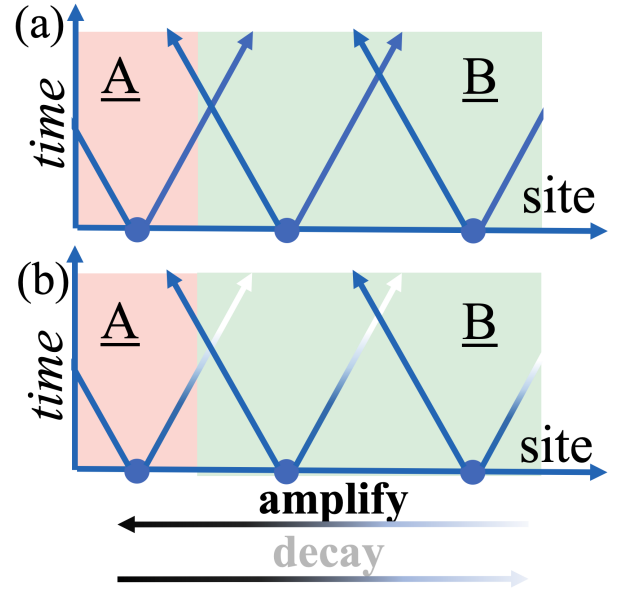


FIG. 1. Schematic illustration of the quasiparticle picture: (a) in the Hermitian case, and (b) in the case of the Hatano-Nelson type asymmetric hopping model (non-Hermitian case).

of hopping (sign of g).⁴² Such a unidirectional motion is robust against disorder and suppresses wave packet spreading (see Supplemental Material 1). This peculiar wave-packet dynamics leads to a remarkable non-monotonic time evolution of the entanglement entropy $S_{\text{ent}}(t)$.⁴³ In the body of the paper, we provide an intuitive explanation on the increase of S_{ent} in the delocalized regime from the viewpoint of the quasiparticle picture.

This work is also an outcome of a technical advancement we have made in our numerics. Here, we have successfully employed the Krylov subspace method⁴⁴ in our problem, which has allowed us to deal with a system of

larger size than the previous studies, e.g., the one of our own.⁴³ This has been particularly helpful in the study of the scaling property of S_{ent} .

The paper is organized as follows. In Sec. II, we introduce the HN model, the numerical conditions, and the definition of entanglement entropy. In Sec. III, we systematically investigate the effect of disorder on the density dynamics in the real and momentum spaces and entanglement dynamics. In Sec. IV, we point out the difference in the entanglement dynamics between the non-Hermitian and Hermitian systems in the clean limit from the perspective of the quasiparticle picture. In Sec. V, we investigate whether non-Hermiticity induces entanglement transition. In Sec. VI, we examine various aspects of S_{ent} , such as its scaling behavior, the effect of interaction, and its relation to the correlation function. Sec. VII is devoted to concluding remarks. Some details are left in the appendices and Supplemental Materials.

II. MANY-BODY HATANO-NELSON MODEL

Let us first introduce our model, which is a many-body extension of the so-called Hatano-Nelson (HN) model,^{39–41} and reads in the second quantization representation as

$$\mathcal{H} = - \sum_{j=0}^{L-1} \left(\Gamma_L c_j^\dagger c_{j+1} + \Gamma_R c_{j+1}^\dagger c_j \right) + \sum_{j=0}^{L-1} \left(V \hat{n}_j \hat{n}_{j+1} + W_j \hat{n}_j \right), \quad (1)$$

where c_j^\dagger (c_j) is a creation (annihilation) operator of a particle at site j , while $\hat{n}_j = c_j^\dagger c_j$ is a number operator which counts the number n_j of such particles found at site j . The first two-terms represent the asymmetric hopping, where the degree of non-reciprocity (asymmetry) is specified by the parameter g

$$\Gamma_L = e^g \Gamma_0, \quad \Gamma_R = e^{-g} \Gamma_0. \quad (2)$$

In the third term, V represents the strength of the nearest neighbor inter-particle interaction, while in the last term, W_j represents the depth of an on-site disorder potential at a site j . Here, unlike in the original Hatano-Nelson model,^{39–41} in which the random numbers W_j 's obey to a uniform distribution, we consider the case in which W_j represents a quasi-periodic potential (cf. the Aubry-André model⁴⁵):

$$W_j = W \cos(2\pi\alpha j + \theta), \quad (3)$$

where α should be chosen to be an irrational number, e.g., $\alpha = (\sqrt{5} - 1)/2$. For α thus chosen, the quasi-periodic potential W_j mimics a random/disorder potential as the one in the original Hatano-Nelson model, W represents the strength of the disorder potential. If an average over

different disorder configurations is necessary, one can activate the parameter θ in Eq. (3), and take the average over θ .

Though the original Hatano-Nelson model [case of $V = 0$ in Eq. (1)] has first appeared^{39–41} as an effective model describing the phenomenon of vortex (de)pinning, it is now considered to be a prototypical non-Hermitian situation, and readapted in a number of different works. The aspect of asymmetric hopping: $g \neq 0$ leads (under the open boundary) to the so-called non-Hermitian skin effect, and is much discussed in the context of the idea of non-Hermitian topological insulator.^{46–57} The competition between the effect of asymmetric hopping: $g \neq 0$ and that of the disorder potential $W \neq 0$ leads to a typical delocalization-localization transition in this non-Hermitian system, and the model is also much discussed in this context.^{58–63} If the localization length ξ is known in the Hermitian limit, the localization transition is expected to occur at $g = \xi^{-1}$ in the corresponding non-Hermitian model.^{39–41} In a non-interacting system, either Hermitian or non-Hermitian, ξ can be calculated by the transfer matrix method.^{64–67} In an interacting system, this is simply not possible, while the study of the interacting Hatano-Nelson model brings about some information on the many-body localization length,^{43,68} since the asymmetric hopping g can be interpreted (under the periodic boundary) as an imaginary flux.⁶⁹

A. Non-Hermitian many-particle dynamics

In the simulation of many-particle dynamics, we will typically consider the initial state:

$$|\Psi(0)\rangle = |\Psi(t=0)\rangle = |101010\cdots\rangle, \quad (4)$$

i.e., the one in the density wave form, or in the Néel form in the spin language.⁷⁰ On the right hand side of Eq. (4), we have employed the computational basis $|n_1 n_2 \cdots n_L\rangle$; $n_j = 0, 1$ represents occupation of the j th site. At time $t = 0$, the initial state (4) can be expressed as a superposition of eigenstates as

$$|\Psi(0)\rangle = \sum_{\alpha} c_{\alpha}(0) |\alpha\rangle, \quad (5)$$

where $|\alpha\rangle$ represents a many-body eigenstate of the Hamiltonian (1), i.e., $\mathcal{H}|\alpha\rangle = E_{\alpha}|\alpha\rangle$. Note that the eigenenergy E_{α} is generally complex. In Eq. (5), $|\alpha\rangle$ represents a right eigenstate corresponding to the eigenenergy E_{α} , which is generally not identical to the Hermitian conjugate of the corresponding left eigenstate $\langle\langle\alpha|$, where

$$\langle\langle\alpha|\mathcal{H} = E_{\alpha}\langle\langle\alpha|, \quad (6)$$

or rather, $\langle\langle\alpha| \neq |\alpha\rangle^\dagger$. To find the coefficients $c_{\alpha}(0)$ in Eq. (5), one actually needs to find such left eigenstates, i.e.,

$$c_{\alpha}(0) = \langle\langle\alpha|\Psi(0)\rangle. \quad (7)$$

Note that the left and right eigenstates satisfy the biorthogonal condition:⁷¹

$$\langle\langle\alpha|\beta\rangle\rangle = \delta_{\alpha,\beta}. \quad (8)$$

We then let the state Eq. (5) evolve into $\Psi(t)$, in principle, via the Schrödinger equation,

$$i\hbar \frac{\partial}{\partial t} |\Psi(t)\rangle = H |\Psi(t)\rangle, \quad (9)$$

though, in practice, we let it evolve through a numerical recipe outlined in the next subsection. In case of a *unitary* time evolution driven by a Hermitian Hamiltonian, the weight of each eigenstate $|\alpha\rangle$ is unchanged in the time-evolved wave packet $|\Psi(t)\rangle$; if one expresses $|\Psi(t)\rangle$ as a superposition of eigenstates as in Eq. (5), or

$$|\Psi(t)\rangle = \sum_{\alpha} c_{\alpha}(t) |\alpha\rangle, \quad (10)$$

the magnitude of the coefficients

$$c_{\alpha}(t) = c_{\alpha}(0) e^{-iE_{\alpha}t} \quad (11)$$

is conserved in the case of unitary time evolution driven by a *Hermitian* Hamiltonian; i.e., in the course of time; $|c_{\alpha}(t)|^2$ are just constants, or $|c_{\alpha}(t)|^2 = |c_{\alpha}(0)|^2$. Here, in the case of *non-unitary* time evolution driven by a *non-Hermitian* Hamiltonian, this is no longer the case; the coefficients $c_{\alpha}(t)$ that appear in Eqs. (10) and (11) change constantly their amplitudes in the time evolution. In such non-unitary time evolution, the total probability $\langle\Psi(t)|\Psi(t)\rangle$ is *a priori* not conserved,⁷² which is, of course, a great problem for the probabilistic interpretation of quantum mechanics, and also a technical problem as well; if the amplitudes diverges, the simulation of wave-packet dynamics becomes awkward. Here, to overcome the difficulty, we take a pragmatic viewpoint that follows the ones of Refs. 42 and 43, etc., by pretending that we are only interested in the relative importance of $c_{\alpha}(t)$ in Eq. (10) with respect to other $c_{\alpha}(t)$'s, and choose to rescale (renormalize) the wave function $|\Psi(t)\rangle$ as

$$|\Psi(t)\rangle \rightarrow |\tilde{\Psi}(t)\rangle = \frac{|\Psi(t)\rangle}{\sqrt{\langle\Psi(t)|\Psi(t)\rangle}}, \quad (12)$$

Then, the *a priori* non-unitary, non-probability-conserving dynamics becomes superficially regularized (normalized).

Here, in the case of *non-Hermitian non-unitary* dynamics, a remarkable fact is that as time passes by, contributions from those $|\alpha\rangle$'s whose eigenenergy has a large positive imaginary part become dominant in the superposition of many eigenstates $|\alpha\rangle$ in Eq. (10); for

$$\text{Im}(E_{\alpha_1}) > \text{Im}(E_{\alpha_2}) > \dots, \quad (13)$$

$$|c_{\alpha_1}(t)|^2 \gg |c_{\alpha_2}(t)|^2 \gg \dots, \quad (14)$$

i.e., only the first few $|\alpha_1\rangle, |\alpha_2\rangle, \dots$ become relevant in the superposition (10) if $|\alpha_1\rangle, |\alpha_2\rangle, \dots$ are labelled in the decreasing order of $\text{Im}(E_{\alpha})$, and if the maximal $\text{Im}(E_{\alpha_1})$ is sufficiently larger than the rest; i.e., if $\text{Im}(E_{\alpha_1}) \gg \text{Im}(E_{\alpha_2})$, in the end of the time evolution ($t \rightarrow \infty$), the wave packet $|\Psi(t)\rangle$ will be completely dominated by a single eigenstate $|\alpha_1\rangle$; i.e., apart from an unimportant phase factor,

$$\lim_{t \rightarrow \infty} |\tilde{\Psi}(t)\rangle \sim |\alpha_1\rangle. \quad (15)$$

Thus, in the non-Hermitian quantum dynamics, the non-unitarity of the time evolution associated with the imaginary part of the eigenenergy gives rise to *collapse of the superposition* of an initial wave packet (5). After a long enough non-unitary time evolution, a generic initial state composed of many different eigenstates tends to converge to a single (or to a few) eigenstate(s).⁷³

B. Numerical simulation

Simulating a many-body quantum system is challenging, since the size of the Hilbert space increases exponentially with the increase of size L of the system. In a simulation of a Hermitian system using the exact diagonalization method, $L = 18$ may be a typical maximal size one can handle comfortably in a present day computer performance. In a non-Hermitian system, however, it is necessary to consider not only the eigenenergy and right eigenvector, but also the left eigenvector. Consequently, most studies are limited to treating system sizes up to $L = 16$.^{43,60,61,70,74,75} Confronted with this numerical challenge, we have decided to employ the Krylov subspace method. In order to make it compatible with a non-Hermitian matrix, we have generated the orthonormal Krylov subspace V_M using the Arnoldi method, instead of the Lanczos method.⁴⁴ The Krylov subspace is given by $K_M = \text{span}(|\Psi(t)\rangle, H|\Psi(t)\rangle, \dots, H^{M-1}|\Psi(t)\rangle)$. The time evolution of quantum state is described by

$$|\Psi(t + \delta t)\rangle \sim V_M e^{-i\delta t H'} V_M^\dagger |\Psi(t)\rangle = V_M e^{-i\delta t H'} |e_1\rangle, \quad (16)$$

where $|e_1\rangle \equiv (1, 0, \dots, 0)^T$ and $H' = V_M^\dagger H V_M$. This allows us to calculate $|\Psi(t + \delta t)\rangle$ by dealing with matrix H' of size $M \times M$ instead of diagonalizing the original Hamiltonian H , and eventually enables us to study a system of larger size than those in the previous studies⁴³. In the actual numerical calculations, we choose $\delta t = 10^{-2} - 2 \times 10^{-1}$ and $M = 10 - 25$.

C. Entanglement entropy: definitions

In the study of many-body dynamics, we are not only interested in how the density spreads but also how correlation spreads in the system. To quantify the latter, we consider the entanglement dynamics. The entanglement

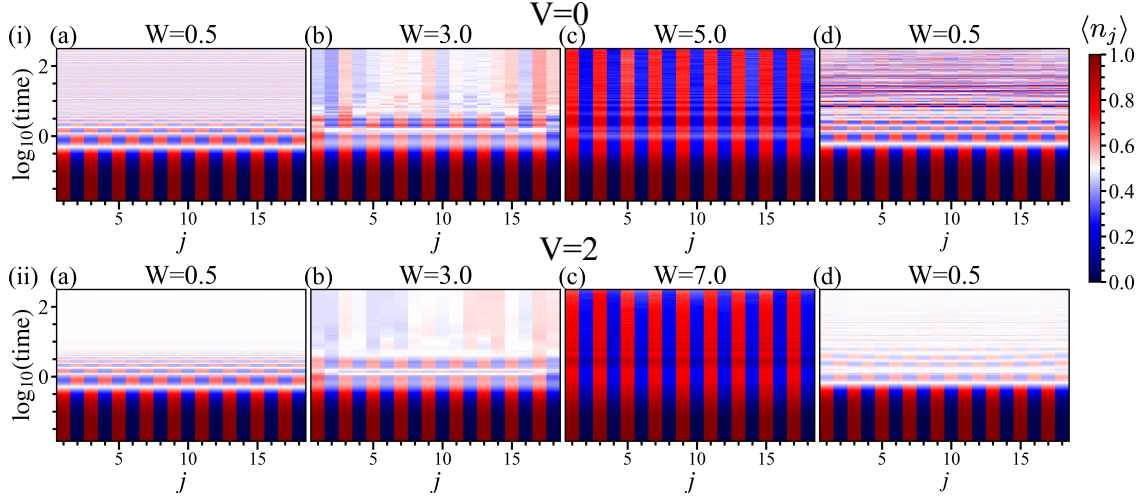


FIG. 2. Time evolution of the spatial profile of the density $n_j(t)$. The first row [(i-a)-(i-c)]: non-interacting case ($V = 0$), asymmetric hopping ($g = 0.5$) and, (i-d): $V = 0$, $g = 0.0$. The second row [(ii-a)-(ii-c)]: interacting case ($V = 2$), $g = 0.5$ and, (ii-d): $V = 2$, $g = 0.0$. In numerical calculation, for $g \neq 0$ we carried out the evaluations with 80 (for $V = 2$) and 40 (for $V = 0$) samples. For Hermitian case, we used 80 samples.

entropy is a quantity to characterize the non-locality of a quantum state, which is often defined in the sense of *bipartite* entanglement entropy:

$$S_{\text{ent}} = -\text{Tr}_A[\Omega_A \log \Omega_A], \quad (17)$$

where

$$\Omega_A = \text{Tr}_B[\Omega] \quad (18)$$

is the reduced density matrix of the subsystem A; we have divided the entire system (of size L) into two subsystems A and B. In practice, such a division can be done using a many-body basis \tilde{n} represented by a set of quantum numbers $\tilde{n} = \{n_1, n_2, \dots, n_L\}$, which can be divided into the two parts as $\tilde{n} = \{\tilde{n}_A, \tilde{n}_B\}$, where $\tilde{n}_A = \{n_1, n_2, \dots, n_\ell\}$ spans the subsystem A, while the remaining part: $\tilde{n}_B = \{n_{\ell+1}, n_{\ell+2}, \dots, n_L\}$ spans the subsystem B. ℓ is the size of the subsystem A. In this basis, a many-body state $|\Psi\rangle$ may be represented as

$$|\Psi\rangle = \sum_{\tilde{n}} \psi_{\tilde{n}} |\tilde{n}\rangle = \sum_{\tilde{n}_A \in A, \tilde{n}_B \in B} \psi_{\tilde{n}_A, \tilde{n}_B} |\tilde{n}_A\rangle |\tilde{n}_B\rangle. \quad (19)$$

Using this, one can explicitly trace out the subsystem B from the density matrix:

$$\Omega = |\Psi\rangle\langle\Psi| = \sum_{\tilde{n}, \tilde{n}'} \psi_{\tilde{n}} \psi_{\tilde{n}'}^* |\tilde{n}\rangle\langle\tilde{n}'|, \quad (20)$$

i.e., the reduced density matrix (18) becomes

$$\begin{aligned} \Omega_A &= \sum_{\tilde{n}_B'' \in B} \langle \tilde{n}_B'' | \Omega | \tilde{n}_B'' \rangle \\ &= \sum_{\tilde{n}_A, \tilde{n}_A' \in A, \tilde{n}_B \in B} \psi_{\tilde{n}_A, \tilde{n}_B} \psi_{\tilde{n}_A', \tilde{n}_B}^* |\tilde{n}_A\rangle\langle\tilde{n}_A'|. \end{aligned} \quad (21)$$

Here, we consider the time evolution of a many-body density matrix: $\Omega(t) = |\Psi(t)\rangle\langle\Psi(t)|$, and the corresponding entanglement entropy $S_{\text{ent}}(t)$.

III. DENSITY AND ENTANGLEMENT DYNAMICS

In this section, we sketch the results of our numerical simulation on the (many-particle) density and entanglement dynamics.

A. Density dynamics in real vs. reciprocal spaces

Let us first focus on the time evolution of the density profile in real space:

$$n_j(t) = \langle\Psi(t)|c_j^\dagger c_j|\Psi(t)\rangle, \quad (22)$$

where $|\Psi(t)\rangle$ actually means $|\tilde{\Psi}(t)\rangle$ in Eq. (12), but to simplify the notation, here, we have omitted the tilde in $|\tilde{\Psi}(t)\rangle$, and we will omit it hereafter. Figure 2 shows the time evolution of $n_j(t)$ for the initial density wave (DW) pattern (4) in the non-interacting ($V = 0$) [first row, panels (i-a)-(i-d)], and in the interacting ($V = 2$) [second row, panels (ii-a)-(ii-d)] cases. In both cases the last panel [(i-d) and (ii-d)] represents the Hermitian case $g = 0$ for comparison. Otherwise, g is chosen as $g = 0.5$ (non-Hermitian). Different panels correspond to the varying strength of disorder: $W = 0.5$ for panels (i-a) and (ii-a), $W = 3.0$ for panels (i-b) and (ii-b), $W = 5.0$ for panels (i-c), and $W = 7.0$ for (ii-c).

In the first column (delocalized phase, $W = 0.5$, panel (i-a) and (ii-a)), the initial density wave pattern tends to

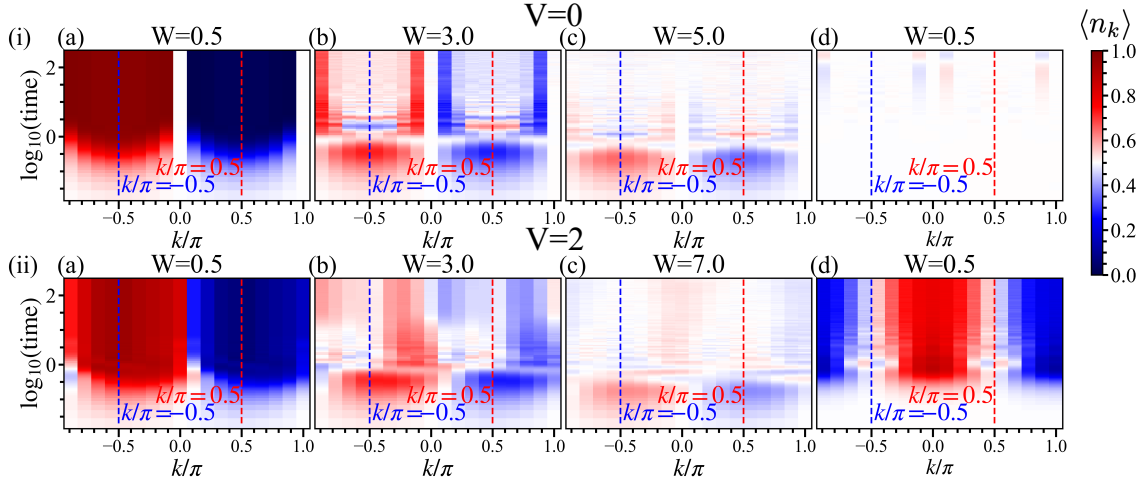


FIG. 3. Evolution of the density profile in the crystal-momentum (k -) space; i.e., $n_k(t)$. Similarly to Fig. 2, the first row [(i-a)-(i-c)]: non-interacting case ($V = 0$), asymmetric hopping ($g = 0.5$), and (i-d): $V = 0$, symmetric hopping ($g = 0.0$). The second row [(ii-a)-(ii-c)]: interacting case ($V = 2.0$), $g = 0.5$ and, (ii-d): $V = 2.0$, $g = 0.0$. We used the same wave functions as in Fig. 2.

be lost in the time evolution, while in the Hermitian case ($V = 0$) [first row, panel (i-d)], the initial spatial profile does not fade but is replaced with a fast temporally oscillatory pattern which is (almost) never washed out; a feature reminiscent of an integrable system in which a perpetual motion on a regular ideal orbital is ensured by the existence of some integrals of motion (conserved quantities). Still, the spatial profile becomes uniform if averaged over time. In the interacting case ($V = 2$) [second row, panel (ii-d)], scatterings induced by the inter-particle interaction mix such regular ideal orbitals and wash out the perpetual motion. After some relaxation time $t_1 \sim 10^0 = 1$ the spatial profile becomes *literally* uniform. The second column [panels (i-b) and (ii-b)] corresponds to the critical (crossover) regime so that the initial density wave pattern remains at least for a relatively long time. As far as these real space features are concerned, the time evolution of the density profile $n_j(t)$ is *not so* different from the Hermitian case [fourth column, panels (i-d) and (ii-d)]. The third column [panel (i-c) and panel (ii-c)] corresponds to the localized phase, where the initial density wave pattern remains over time, effectively similar to the localized phase in the Hermitian case.

Figure 3 shows time evolution of the density distribution:

$$n_k(t) = \langle \Psi(t) | c_k^\dagger c_k | \Psi(t) \rangle, \quad (23)$$

in the reciprocal crystal-momentum space (k -space), where

$$c_k = \sum_j c_j e^{ikj}. \quad (24)$$

As in Fig. 2, it shows the evolution of $n_k(t)$ both in the non-interacting ($V = 0$) [first row, panels (i-a)-(i-d)] and

in the interacting ($V = 2.0$) [second row, panels (ii-a)-(ii-d)] cases. In both cases the last panel (i-d) and (ii-d) represent the Hermitian case $g = 0$ for comparison; otherwise, $g = 0.5$. Different panels correspond to the varying strength of disorder: $W = 0.5$ for panels (i-a) and (ii-a), $W = 3.0$ for panels (i-b) and (ii-b), $W = 5.0$ for panels (i-c), and $W = 7.0$ for (ii-c).

First, unlike in the real space (Fig. 2) the time evolution of the density profile shows very different features in the Hermitian [column (d)] and non-Hermitian [especially, first two columns: (a) and (b)] cases. In these columns, one can see that as time evolves, the density distribution $n_k(t)$ in the reciprocal space tends to converge to a certain asymptotic distribution, implying that in the regime of sufficiently long time $t \gg 1$, the many-body wave packet $|\Psi(t)\rangle$ tends to approach to a single eigenstate $|\alpha_1\rangle$ as in Eq. (15); in the non-interacting case ($V = 0$, e.g., in the first row of Fig. 3) and also at $W = 0$ $|\alpha_1\rangle$ will be given as

$$|\alpha_1\rangle = \left(\prod_{k<0} c_k^\dagger \right) |0\rangle, \quad (25)$$

implying a sharp Fermi-sea like asymptotic density distribution $n_k^{(\infty)} = n_k(t \rightarrow \infty)$ such that

$$n_k^{(\infty)} = \begin{cases} 1 & \text{for } k < 0 \\ 0 & \text{for } k > 0 \end{cases}. \quad (26)$$

Such a density distribution $n_k(t)$ localized in the crystal-momentum space prevails in the regime of weak disorder also in the case of weak inter-particle interaction; e.g., case of Fig. 3 (ii) (a). As W is increased, e.g., in panel (b) the distribution is smeared out, and a sharp signature as in Eq. (26) becomes no longer visible. Note that in the crystal momentum space, both on-site potential W_j

and the inter-particle interaction V are sources of scattering. V corresponds to two-particle scattering process; two particles with wave number k and k' exchange their momenta. These are all very different from the Hermitian case [column (d)] where $n_k(t)$ remains uniform during the time evolution in the non-interacting case [panel (i-d)], while in the second row [panel (ii-d)], $n_k(t)$ evolves into an equilibrium distribution, which is reminiscent of the one realized in the thermodynamic limit [cf. eigenstate thermalization hypothesis (ETH)]. Inter-particle scatterings induced by a finite V introduces (an effective form of) dissipation in the system (i.e., in the eigenstate), bringing it to an effective thermal equilibrium.

B. Entanglement dynamics

Figure 4 shows examples of entanglement dynamics at various strength of disorder and in systems of different size. The asymmetry in hopping is fixed at $g = 0.5$. Panel (a) represents the non-interacting case ($V = 0$), while in panel (b) a moderate strength of inter-particle interaction ($V = 2.0$) is assumed. In the insets of the two panels different curves represent time evolution of the entanglement entropy S_{ent} at different strength of disorder W but for a system of size fixed at $L = 18$.

In the non-interacting case [panel (a)], the critical strength of disorder W_c for the localization transition is $W_c = 2e^g \simeq 3.297...$, so that

- (i) $W = 0.5, 1.0, 2.0$ correspond to the regime of weak disorder and delocalized wave function,
- (ii) $W = 3$ roughly corresponds to the critical disorder strength W_c , therefore, may be classified into the critical regime, while
- (iii) $W = 4.0, 5.0$ fall on regime of strong disorder and localized wave functions.

In the interacting case, the corresponding values of W in each regime depends on the strength of the interaction V , since in principle, W_c depends on V . In case of panel (b); i.e., at $V = 2.0$, the classification may be such that regime (i): $W = 0.5, 1.0, 2.0$, regime (ii): $W = 3.0, 4.0, 5.0, 6.0$, regime (iii): $W = 7.0, 8.0$. In the main panel, the size dependence of the entanglement entropy is shown in each of the three different regimes.

In the non-interacting case; in panel (a), main panel, after the initial growth $t > 10^0 - 10^1$, $S_{\text{ent}}(t)$ tends to become saturated; in regime (i) to a value $\simeq 1.5$, while in regime (ii) this value is much enhanced, and in regime (iii) the saturated value gets back to the ones comparable to those in regime (i). Thus, as the strength W of disorder is varied (increased), the saturated value of the entanglement entropy changes non-monotonically; it is first enhanced by W , then suppressed.

In the interacting case [panel (b)], the behavior of S_{ent} in regime (i) is similar to the non-interacting case, while the behavior of S_{ent} changes qualitatively in regimes (ii) and (iii). In regime (ii), $S_{\text{ent}}(t)$ is much enhanced in the intermediate time range $t \sim 10^0 - 10^1$, but tends

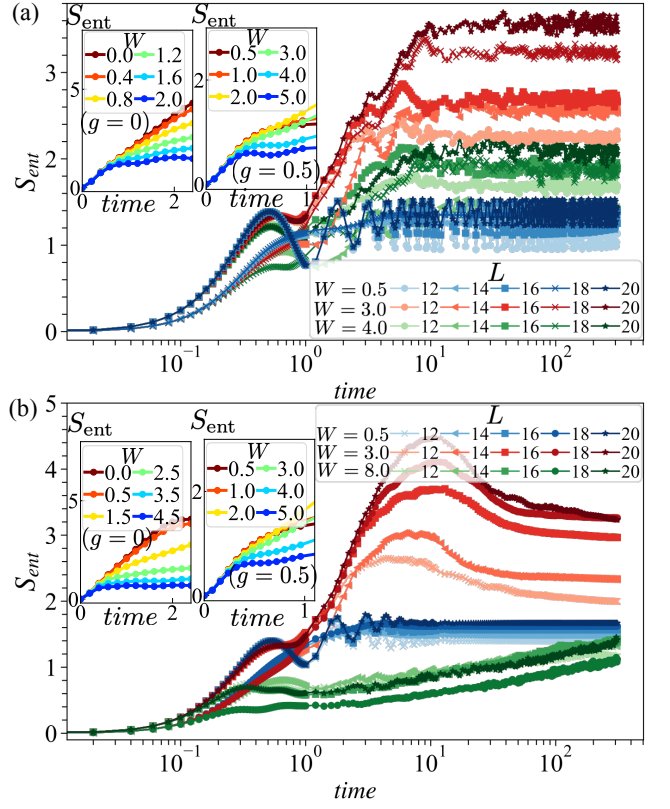


FIG. 4. Entanglement dynamics in three different regimes of disorder strength: delocalized, critical and localized regimes. Size dependence of the entanglement entropy is also shown. (a) non-interacting case: $V = 0$, (b) interacting case: $V = 2$. In numerical calculation, we carried out evaluations for different system sizes using varying sample sizes for $V = 2$. We employed 100, 100, 100, 80, and 40 samples for $L = 12, 14, 16, 18$, and 20, respectively. Similarity, for $V = 0$, we used 100, 40, 40, 40, and 20 samples for $L = 12, 14, 16, 18$, and 20. In inset panels of panel (a), we conducted evaluations for $L = 18$ with 80 samples (for Hermitian case) and 40 samples (for non-Hermitian case). In inset panels of panel (b), we conducted evaluations for $L = 18$ with 80 samples (for both Hermitian and non-Hermitian cases).

to be suppressed afterwards $t > 10^2$; $S_{\text{ent}}(t)$ shows a non-monotonic growth in this regime. In regime (iii) $S_{\text{ent}}(t)$ continues to grow after the initial growth: i.e., $S_{\text{ent}}(t) \sim \log t$ at $t \gg 10^0$; behavior characteristic to the many-body localized regime.^{76–80} Thus, as the strength W of disorder is varied (increased), the overall magnitude of $S_{\text{ent}}(t)$ in its dynamics is again non-monotonic as in the non-interacting case. This is quite a curious behavior if we recall that in the Hermitian case many-body states become less entangled with the increase of W .^{81,82} Here, the many-body states tend to become more entangled with the increase of W , i.e., in the weakly disordered regime (i), while they tend to become less entangled beyond a certain critical value $W > W_c$ [in regime (iii)]. Such non-monotonic dependence on W is a characteristic non-Hermitian feature. In the critical regime [regime

(ii)], on the other hand, another non-monotonic feature is emergent in the entanglement dynamics; i.e., the non-monotonic time evolution of the entanglement entropy $S_{\text{ent}}(t)$ in time.

IV. THE QUASIPARTICLE PICTURE

The entanglement dynamics in a Hermitian system and in (or close to) the clean limit ($W = 0$) is well described by the quasiparticle picture. Here, we discuss, how the entanglement dynamics in a non-Hermitian system we have sketched in the previous section can or cannot be compatible with this picture.

The observed behavior of the density dynamics in the crystal momentum space introduced earlier (see Sec. III) is directly relevant to the description of the quasiparticle picture. In Fig. 3 and related descriptions, we have seen that $\langle n_k \rangle$ is almost uniform ($\langle n_k \rangle \simeq 1/2$) in the Hermitian case, while $\langle n_k \rangle$ converges to $\langle n_k \rangle = 1$ for $k < 0$, and $\langle n_k \rangle = 0$ for $k > 0$ in the non-Hermitian case. The two panels of Fig. 1 are in a sense a pictorial representation of these contrasting behaviors, i.e., Fig. 1, panel (a) corresponds to Fig. 3, panel (i-d); the Hermitian case, and Fig. 1, panel (b) corresponds to Fig. 3, panel (i-a); the non-Hermitian case (close to the clean limit).

A. GGE vs. non-unitary dynamics

Let us focus on the clean limit. First, in the Hermitian case. In this case, $\hat{n}_k = c_k^\dagger c_k$ is a conserved quantity: $[\hat{n}_k, H] = 0$. In this integrable system, the expectation value, such as $\langle \hat{n}_k \rangle = \langle \Psi | \hat{n}_k | \Psi \rangle$ is also expressed as a statistical average in the so-called generalized Gibbs ensemble (GGE); see Appendix A for details. characterized by an infinite number of Lagrange multipliers λ_k , each associated with the conservation of n_k . To be explicit, n_k can be expressed as

$$\langle \hat{n}_k \rangle = \frac{1}{1 + e^{\lambda_k}}, \quad (27)$$

where for the density-wave like initial state (4) all λ_k are equal to 0,⁸³ i.e., $\langle \hat{n}_k \rangle = 1/2$. We have seen this in the density dynamics studied in Sec. III. In Fig. 3, in all the panels, the initial and early time density distribution $n_k(t = 0)$ shows such a uniform profile ($\langle \hat{n}_k \rangle \simeq 1/2$), while in the first row, panel (i-d), i.e., in the non-interacting ($V = 0$) and Hermitian ($g = 0$) case, such an initial profile is maintained, though approximately, due to a small but finite $W = 0.5$. Note that the (entanglement) entropy associated with a generalized Gibbs ensemble specified by the distribution (27) is given as (see Appendix A for its derivation)

$$s(k) = -\langle \hat{n}_k \rangle \log(\langle \hat{n}_k \rangle) - (1 - \langle \hat{n}_k \rangle) \log(1 - \langle \hat{n}_k \rangle). \quad (28)$$

Note that this takes a maximal value $\log 2$ at $\langle \hat{n}_k \rangle = 1/2$ ($\lambda_k = 0$).

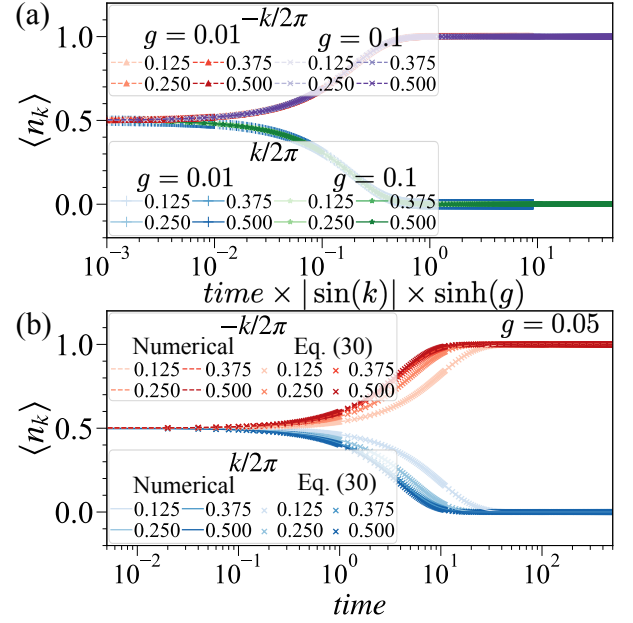


FIG. 5. Time-dependence of $\langle \hat{n}_k \rangle$: (a) $\langle \hat{n}_k \rangle$ versus $\text{time} \times \sin(k) \times \sinh(g)$ with the various values of g , (b) $\langle \hat{n}_k \rangle$ (scatter plot) and Eq. (30) (solid or dashed line) versus time . For panels (b), g is fixed at $g = 0.05$. Numerical calculation is conducted by the following parameter: $L = 16$, $W = 0$, and $V = 0$.

In the *non-Hermitian* case with $\text{Im}(\epsilon_k) \neq 0$ (ϵ_k is a single particle eigenenergy), if we repeat the same argument leading to Eq. (27), one is left with (see Appendix A)

$$\langle \hat{n}_k \rangle = \frac{1}{1 + e^{\lambda_k - 2\text{Im}(\epsilon_k)t}}, \quad (29)$$

i.e., $\langle \hat{n}_k \rangle$ is no longer conserved in this case. Again, for the initial DW like pattern (4), all λ_k 's are to be set to 0 in Eq. (29). Noticing that $\text{Im}(\epsilon_k) > 0$ for $k < 0$, $\text{Im}(\epsilon_k) < 0$ for $k > 0$, and thus $\langle \hat{n}_k \rangle$ converges either to 0 ($k > 0$) or to 1 ($k < 0$). In Fig. 5, we have plotted the calculated value of $n_k(t)$ against the scaling function

$$\langle \hat{n}_k \rangle = \frac{1}{1 + e^{-2\text{Im}(\tilde{\epsilon}_k)t}}, \quad (30)$$

where $\tilde{\epsilon}_k = 2\epsilon_k$. Figure 5 shows that the numerical data fit quite well with the scaling function (30) expected in GGE except for a factor 2 in the definition of $\tilde{\epsilon}_k$.⁸⁴

As shown also in a more generic context in Appendix A [see, e.g., Eqs. (A4) and (A5)], the time dependence of $\langle \hat{n}_k \rangle$ [here, e.g., Eq. (29)] is analogous to that of the imaginary time evolution driven by a *Hermitian* Hamiltonian, often employed in a numerical recipe to find the ground state, e.g., in a path-integral quantum Monte Carlo, or in a tensor-network method.⁸⁵ In the imaginary time evolution, the parameter, t (time) corresponds to a “temperature” of the statistical ensemble. Thus, an evolution driven by a non-Hermitian matrix leads to an effective decrease in temperature. Consequently, as time passes by,

the temperature decreases, and the entropy (S_{ent}) also seems to decrease. In the following subsection, we investigate how S_{ent} behaves under a non-unitary dynamics.

B. Entanglement dynamics in the quasiparticle picture

In the quasiparticle picture, the initial state $|\Psi(t=0)\rangle$ consists of a superposition of a highly excited state, acting as a source of quasi-particle excitations. Pairs of quasiparticles with opposite momenta k and $-k$ are emitted at the same point, and as times passes by, they move, in the Hermitian case, symmetrically in opposite directions. This is schematically depicted in panel (a) of Fig. 1. Once each quasiparticle is located in the different subsystem, S_{ent} increases. This process is formulated by

$$S_{\text{ent}}(t) \propto 2t \int_{2v(k)t < \ell} dk v(k) s(k) + \ell \int_{2v(k)t > \ell} dk s(k), \quad (31)$$

where ℓ is the subsystem size, k is a momentum of quasiparticles, $v(k)$ is its velocity, and $s(k)$ determines the production rate of S_{ent} . This production rate tightly relates to the entropy of statistical mechanics because $s(k) = -\langle \hat{n}_k \rangle \log(\langle \hat{n}_k \rangle) - (1 - \langle \hat{n}_k \rangle) \log(1 - \langle \hat{n}_k \rangle)$.

Entanglement dynamics (31) has a characteristic time scale $t_c(k)$ determined by ℓ and $v(k)$. When $t_c(k) \equiv \frac{\ell}{2v(k)} > t$, each quasiparticles emitted at the same points begin to be located in the different subsystems, contributing to the entanglement production as a function of $s(k)v(k)t$. While $t_c(k) < t$, most of each quasiparticles are located in the different subsystems; therefore, the contribution of S_{ent} from pairs of quasiparticles $s(k)$ becomes constant value $s(k)\ell$.⁸⁶

In the non-Hermitian case, as time passes by, one of the quasiparticles is amplified while the other is attenuated due to $\text{Im}(E)$, resulting in a unidirectional motion (depicted in panel (b) of Fig. 1). Moreover, this characteristic relaxation of $\langle \hat{n}_k \rangle$ (30) results in a variation of $\langle \hat{n}_k \rangle$ from $\langle \hat{n}_k \rangle = 0.5$, indicating a decrease in S_{ent} as suggested by Eqs. (30) and (31). Therefore, we investigate how the non-Hermiticity, specifically this characteristic relaxation, modifies the quasiparticle picture and entanglement dynamics. Panels (a) and (b) of Fig. 6 show S_{ent} as a function of time and $\text{time} \times \cosh(g)$, respectively, with various values of g . We observe distinct behaviors of $S_{\text{ent}}(t)$ arising from the quasiparticle picture and non-unitary time evolution. We first focus on the initial growth of S_{ent} . According to the quasiparticle picture, the initial growth of S_{ent} depends on $v_g t$ (v_g is a group velocity, and see Eq. (31) rather than $e^g t$ since S_{ent} is carried by quasiparticles as well as correlation. In this case, $v_g = -2 \cosh(g) \sin(k)$, and thus we expect that the initial growth of S_{ent} depends on $\cosh(g) \sin(k)t$. We observe that the initial growth of S_{ent} can be approximated by a single curve, as is shown in panel (b), consistent with the quasiparticle picture and implying the validity of the

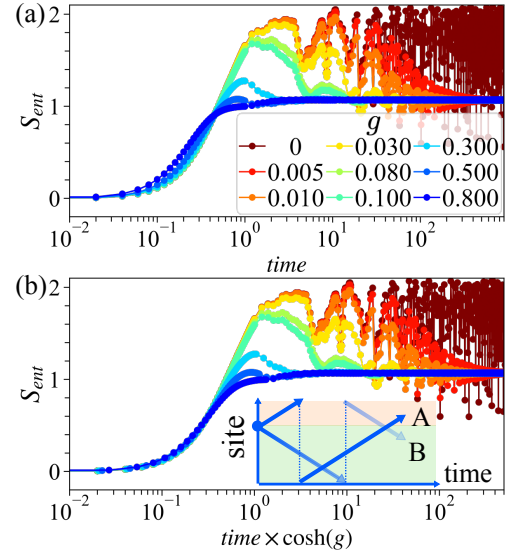


FIG. 6. Entanglement dynamics of a free particle case with $\ell = 3$ with decrease of g : (a) S_{ent} versus time and (b) S_{ent} versus $\text{time} \times \cosh(g)$ (analogy of quasiparticle picture). $L = 16$

quasiparticle picture at early time scales. Following the initial growth, $S_{\text{ent}}(t)$ depends on g . $S_{\text{ent}}(t)$ shows non-monotonic behavior for weak g , whereas it only converges to S_{ent} of $|\alpha_1\rangle$ for strong g . This difference in $S_{\text{ent}}(t)$ between weak and strong g stems from the relaxation of $\langle \hat{n}_k \rangle$. For weak g , Eq. (30) implies that the relaxation of $\langle \hat{n}_k \rangle$ takes a considerable amount of time, causing $S_{\text{ent}}(t)$ to resemble the behavior observed in the Hermitian case within this regime, leading to $S_{\text{ent}}(t) > S_{\text{ent}}(t \rightarrow \infty)$. However, $\text{Im}(E)$ eventually causes $\langle \hat{n}_k \rangle$ to converge to either 0 or 1, thereby resulting in the convergence of $S_{\text{ent}}(t)$ to $S_{\text{ent}}(\infty)$ and non-monotonic behavior of S_{ent} .⁸⁷ Additionally, we also observe Hermitian-like behavior in which the non-monotonic behavior of S_{ent} is accompanied by oscillations. These oscillations occur when quasiparticles move through the left or right ends (see inset of panel (b) of Fig. 6) and are located within the same subsystem. This oscillation behavior is known for entanglement revivals⁸⁸, predicted by the quasiparticle picture. For large g , $\langle \hat{n}_k \rangle$ immediately converges to either 0 or 1, and thus $S_{\text{ent}}(t)$ only converges to $S_{\text{ent}}(\infty)$.

As we have observed, the interplay between the quasiparticle picture and the relaxation described by Eq. (30) qualitatively captures entanglement dynamics of the HN model. In Appendix (C), we compare the numerical result with S_{ent} suggested by the quasiparticle picture to verify the accuracy of this picture. While this picture provides a qualitative characterization of $S_{\text{ent}}(t)$, we find a quantitative discrepancy between the numerical result and S_{ent} suggested by this picture. Further work is required to identify the reason why this quantitative discrepancy presents.

C. Disordered case: disorder enhances the entanglement

The quasiparticle picture also provides us with a natural interpretation on why disorder enhances the entanglement in the non-Hermitian case. First, in the Hermitian case, as disorder is introduced to the system, here in our analysis, in the form of a quasi-periodic potential, the entanglement entropy tends to be suppressed; see e.g., inset of Fig. 4. This is because such a quasi-periodic potential introduces scattering between quasiparticles, preventing quasiparticle pairs from reaching a different subsystem [Fig. 1, panel (a)]. If the pairs tend to stay in the same subsystem, the entanglement entropy tends naturally to be decreased. In the non-Hermitian case, scattering between quasiparticles introduced by the quasi-periodic potential may lead to quite a different consequence. As repeatedly mentioned, the quasiparticle motion is unidirectional in the absence of scattering [Fig. 1, panel (b)], while in the presence of scattering this is expected to be no longer purely uni-directional, but become more bi-directional. As a result, disorder helps quasiparticle pairs to reach a different subsystem, leading naturally to the increase of entanglement entropy.

In the density dynamics (Fig. 3), we have seen that $\langle n_k \rangle$ converges sharply to 0 or 1 in the clean limit, while in the presence of disorder, this convergence is relaxed. This clearly leads to the increase of thermodynamic entanglement entropy: Eq. (28) (see Appendix A for more details). In the interacting case, the behavior of $\langle n_k \rangle$ is not much different from the non-interacting case [Fig. 3, panel (ii)], the above reasoning in the non-interacting case applies also, at least qualitatively, to the interacting case.

Previously, we have attributed this enhancement of the entanglement entropy due to disorder to cascade-like spreading of the wave packet in the single-particle dynamics.^{43,89} Here, we have shown that the quasiparticle picture gives a more natural explanation of the same phenomenon, which is more likely valid in the interacting case.

V. LOGARITHMIC SCALING IN THE ASYMPTOTIC REGIME: $t \rightarrow \infty$

In the previous subsection, we have seen characteristic behaviors of the entanglement entropy $S_{\text{ent}}(t)$, which reflects the collapse of the superposition in the time-evolving many-body state $|\Psi(t)\rangle$; i.e., its convergence to a single eigenstate (15). In the Hermitian system, the asymptotic value of the entanglement entropy,

$$S_{\infty} = S_{\text{ent}}(t \rightarrow \infty), \quad (32)$$

obeys the volume-law scaling. Here, we address what type scaling S_{∞} shows in the non-Hermitian case. For a given entire system of size L ; here, we fix it at $L = 20$, we vary the bipartite division ℓ , i.e., the size of the subsystem

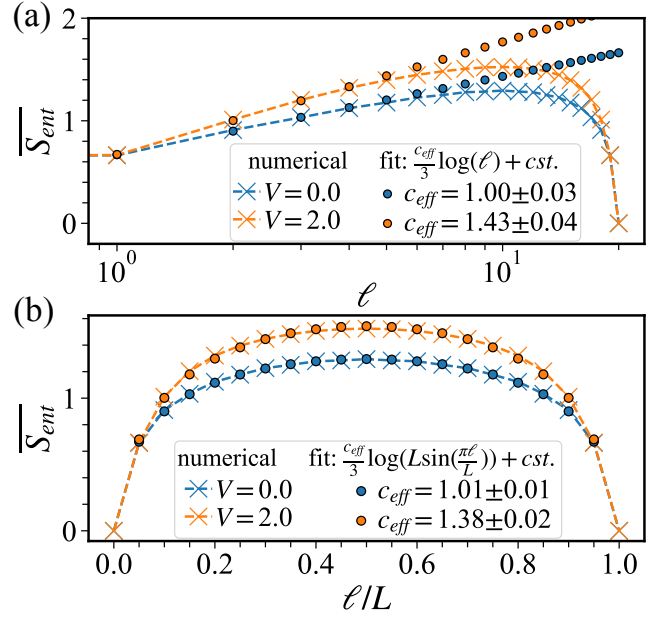


FIG. 7. Scaling of S_{ent} as a function of ℓ , where ℓ is a length of subsystem: (a) S_{ent} versus ℓ , (b) S_{ent} versus ℓ/L . For panel (b), we take into account the boundary condition, so that fitting function $\frac{c_{\text{eff}}}{3} \log(L \sin(\frac{\pi \ell}{L})) + cst.$ (scatter plot) seems to be fitted the numerical data (dashed line). $cst.$ is corresponding to a constant value.

A, and evaluate the entanglement entropy $S_{\infty}(\ell)$ in the asymptotic regime $t \rightarrow \infty$. Fig. 7 (a) shows a result of such analyses in the case of $W = 0$, $V = 0$, in which $S_{\infty}(\ell)$ is plotted against $\log \ell$. One can see that for $\ell \ll L$ at which size effects are negligible, the entanglement entropy $S_{\infty}(\ell)$ is well fit by the scaling function:

$$S_{\infty}(\ell) = \frac{1}{3} \log \ell + cst., \quad (33)$$

known in the Hermitian case for a fermionic ground state, which falls on the case of central charge $c = 1$ (case of free bosonic excitation spectrum).^{90–95}

One can even improve the fitting by taking into account the finite size of the system and the periodic boundary condition; replacing the length ℓ of the subsystem A in Eq. (33) with the corresponding chord distance:

$$d(\ell) = 2L \sin(\pi \ell / L) \quad (34)$$

of a circle of circumference L , one finds

$$S_{\infty}(\ell) = \frac{1}{3} \log [2L \sin(\pi \ell / L)] + cst. \quad (35)$$

In Fig. 7 (b) the same data of the entanglement entropy S_{ent} is plotted against the subsystem size ℓ in linear scale and fit by the scaling function (35). One can see all the data: $\ell = 1, 2, \dots, L-1$ of S_{ent} is well fit by this modified scaling function.

In case of the fermionic ground state,

$$|\Psi_G\rangle = \left(\prod_{k.s.t. |k| < k_F} c_k^\dagger \right) |0\rangle, \quad (36)$$

the logarithmic term in Eq. (33) stems from discontinuities in the momentum space at $k = k_F$ and $k = -k_F$, where k_F is the Fermi wave number or Fermi (crystal) momentum associated with the Fermi energy $\epsilon_F = \hbar^2 k_F^2 / (2m)$. In the asymptotic expansion for large L , the sub-leading logarithmic term becomes relevant as a result of the vanishing of the leading linear term $\propto L$ (volume-law term). In the non-Hermitian dynamics the many-body wave packet $|\Psi(t)\rangle$ may converge to a single eigenstate (25). Then, the corresponding momentum distribution (26) exhibits discontinuities at $k = 0$ and $k = -\pi$ in case of the half-filling. These discontinuities lead to logarithmic scaling of the entanglement entropy (33), known in the fermionic ground state.^{96,97}

In the interacting case, the entanglement entropy $S_\infty(\ell)$ seems still logarithmic [Fig. 7, panel (b)], in the sense that the data is well fit by the following scaling function:

$$S_\infty(\ell) = \frac{c_{\text{eff}}}{3} \log [2L \sin(\pi\ell/L)] + \text{cst.}, \quad (37)$$

where c_{eff} is a fitting parameter; of course, the naming implies that we are tempted to interpret it as an effective central charge. Our data clearly shows that c_{eff} exhibits deviation from the non-interacting value $c = 1$. As a remark, the way it deviates from $c = 1$ in the present case is opposite to the Hermitian case.⁹⁸ Another remark is that in the regime of larger V we found a discrepancy of our data with the fitting function (37); see Appendix D for more details. The discrepancy may be simply due to a finite size effect, but in any case a further investigation in a system of larger size L will be necessary, employing the methods such as Bethe ansatz,^{99–101} the tensor-network,^{101–105} and the quantum Monte-Carlo simulation.^{106–109}

VI. FURTHER SCALING PROPERTIES: BEHAVIOR OF $\text{Im}(E)$ AND CORRELATION FUNCTION

A. Imaginary part of the eigenenergy; origin of the non-monotonic time evolution

In Sec. III, we have seen that the entanglement entropy $S_{\text{ent}}(t)$ exhibits a non-monotonic time evolution, typically, in the regime of intermediate disorder and in the interacting case [Fig. 4 (b)]. A sensible reader would immediately associate this intriguing behavior, unique also to the non-Hermitian case, with the complex nature of the spectrum characteristic to the system, which is indeed the case. While, if that is simply the reason, one may then wonder why the non-monotonic evolution is

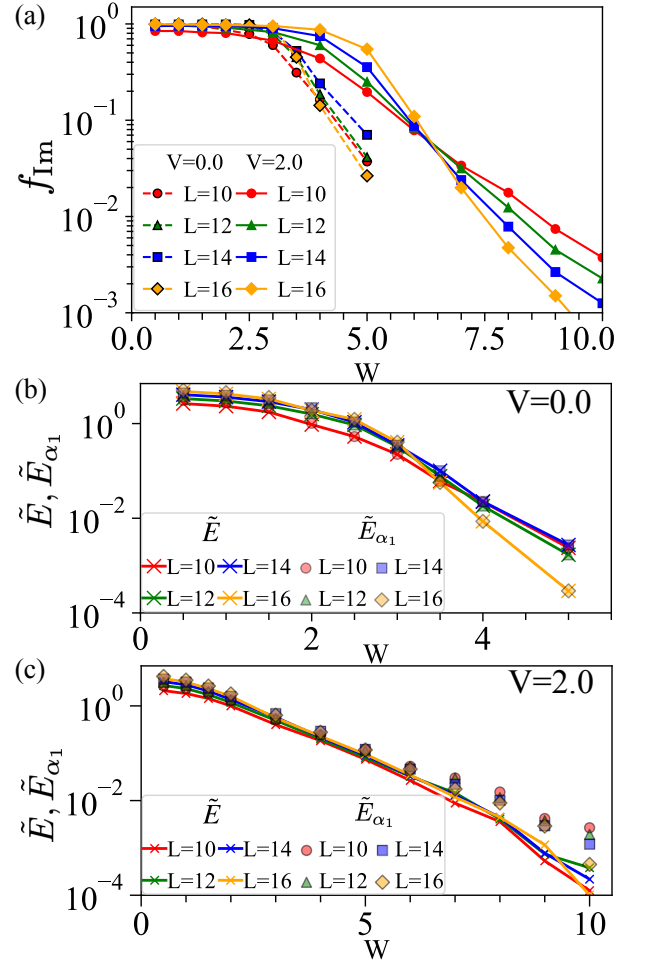


FIG. 8. Disorder dependence of the quantity to characterize the property of $\text{Im}(E)$ for various system sizes L . (a) f_{Im} for non-interacting ($V = 0$, dashed line) and interacting ($V = 2$, solid line) cases, respectively. The largest $\text{Im}(E)$, $\tilde{E}_{\alpha_1} \equiv \text{Max}(\text{Im}(E))$ (scatter plot), and the average value of $\text{Im}(E)$ taken from the 2nd to 5th, \tilde{E} (solid line) for non-interacting (panel (b)) and interacting (panel (c)) cases, respectively. In numerical calculation, we carried out evaluations for various system sizes $L = 12, 14, 16$, and 20 using varying sample sizes: 1000, 500, 500, and 200 samples for $L = 12, 14, 16$, and 16.

specific to the interacting case, and does not appear in the non-interacting case [Fig. 4, panel (a)], albeit that the complex spectrum also appears in non-interacting case. Below, we will carefully focus on the complex nature of the spectrum, highlighting especially the degeneracy in the imaginary part of the spectrum $\text{Im}(E)$. The crucial difference that also leads to the conspicuous difference in the behavior of entanglement entropy $S_{\text{ent}}(t)$ in the interacting vs. non-interacting cases lies in the difference (absence vs. presence) of such degeneracy in $\text{Im}(E)$ in the complex spectrum. After briefly looking into the scaling of the Im ratio f_{Im} , relevant to the identification of the real-complex transition in spectrum, we will proceed to

a more careful study of such degeneracies in $\text{Im}(E)$.

The fraction f_{Im} , which is defined as the ratio of the number of the eigenenergy with non-zero imaginary part ($|\text{Im}(E)| > 10^{-10}$) D_{Im} to the total number of the eigenenergy D ; i.e.,

$$f_{\text{Im}} = D_{\text{Im}}/D, \quad (38)$$

is often employed in the study of real-complex transition.^{62,74} f_{Im} is typically averaged within a defined energy range or across the entire spectrum. Thus, we can consider f_{Im} as a measure to describe the statistical properties of a complex spectrum. In the delocalized phase, f_{Im} is close or almost equal to 1, whereas it practically vanishes in the localized phase. f_{Im} in the non-interacting case shown in Panel (a) of Fig. 8 (dashed line) take almost constant value $f_{\text{Im}} \sim 1$ for weak W , and as W approaches $W_c \sim 3.3$, f_{Im} sharply decreases. This tendency becomes more enhanced as L increases, and in the (W, f_{Im}) -plane, different curves for f_{Im} calculated at different system size L looks intersecting at a single point, $(W_c, f_{\text{Im}}(W_c))$ [Fig. 8, panel (a)], implying that this real-complex transition at $W = W_c$ is a true phase transition robust until the thermodynamic limit: $L \rightarrow \infty$. In the interacting case (solid line), the position of the crossing is shifted to a regime of larger W compared with the non-interacting case (dashed line), while the overall behavior is unchanged from the non-interacting case. Thus, so far as the scaling analysis of f_{Im} implies, the real-complex transition of the spectrum occurs practically in the same way both in the interacting and non-interacting cases. Then, how could that be compatible with a relatively different dynamics of the entanglement entropy $S_{\text{ent}}(t)$ in the interacting and non-interacting cases?

In Sec. II A, we have argued that in the non-unitary time evolution the many-body wave packet $|\Psi(t)\rangle$, which is initially a superposition of many eigenstates, tends to lose such a superposed nature, and collapse into a single eigenstate $|\alpha_1\rangle$ [see Eq. (15)], where $|\alpha_1\rangle$ is such an eigenstate whose eigenenergy E has a maximal imaginary part, $\text{Im}(E)$. This picture demonstrated in Sec. II A is, however, slightly oversimplified in the sense that it did not consider the case in which some eigenstate have (practically) the same, or very close $\text{Im}(E)$; the case in which

$$\text{Im}(E_{\alpha_1}) \simeq \text{Im}(E_{\alpha_2}) \simeq \cdots \quad (39)$$

Which quantity is relevant for determining how quickly the state $|\Psi(t)\rangle$ converges (or not) to a single eigenstate $|\alpha_1\rangle$? $\text{Im}(E_{\alpha_\nu}) > 0$ amplifies the amplitude of the coefficient $c_{\alpha_\nu}(t)$, expressed as $|c_{\alpha_\nu}(t)|^2 = |c_{\alpha_\nu}(t=0)e^{\text{Im}(E_{\alpha_\nu}t)}|^2$. The relative importance of the state $|\alpha_1\rangle$ with respect to another state, e.g., $|\alpha_\nu\rangle$ in the time-evolving wave packet $|\Psi(t)\rangle$ may be quantified by the ratio:

$$\frac{|c_{\alpha_\nu}(t)|^2}{|c_{\alpha_1}(t)|^2} \propto |e^{\text{Im}(2(E_{\alpha_\nu}-E_{\alpha_1})t)}| = e^{-\Delta_{\text{Im}}^\nu t}. \quad (40)$$

Here, we consider the quantity, \tilde{E} defined as the average of the 2nd to the fifth largest value of $\text{Im}(E)$, and conjecture that the difference between $\tilde{E}_{\alpha_1} \equiv \text{Max}(\text{Im}(E))$ would be a good measure for characterizing how quickly the state $|\Psi(t)\rangle$ converges to (or not to) a hypothetical asymptotic state $|\alpha_1\rangle$.

Panels (b) and (c) of Fig. 8 show \tilde{E}_{α_1} and \tilde{E} as a function of W in non-interacting and interacting case, respectively. Both \tilde{E}_{α_1} and \tilde{E} decrease with an increase of W , leading to a decrease in Δ_{Im}^ν (cf. Eq. (40)). Interestingly, in the localized phase of the non-interacting system, \tilde{E} is the same as \tilde{E}_{α_1} , which means \tilde{E}_{α_1} is degenerate. When \tilde{E}_{α_1} is degenerate, the corresponding eigenstates are amplified under time evolution similarly, i.e., $\Delta_{\text{Im}}^\nu = 0$, and thus superposition $c_{\alpha_\nu}(t)$ is maintained (cf. Eq. (40)) even in the non-unitary time evolution. Such a degeneracy stems from the fact that $\text{Im}(E_{\alpha_\nu})$ is a sum of single particle eigenenergy ϵ_α . In the localized phase, most of ϵ_α are real spectra, but some ϵ_α have non-zero imaginary parts of eigenenergy due to the finite system size effect, causing the combination of the sum of the real and complex spectrum to leads to the degeneracy of $\text{Im}(E)$. In contrast to the non-interacting case, in an interacting case, \tilde{E}_{α_1} is not the same as the \tilde{E} , which means that $|\Psi(t)\rangle$ generally converges to a single eigenstate $|\alpha_1\rangle$ and non-monotonic behavior of S_{ent} appears consequently.

B. Entanglement entropy and correlation function

Finally, we focus on how the scaling of the entanglement entropy S_{ent} and the correlation function as a function of the strength W of disorder. In Panel (a) of Fig. 9, $S_\infty = S_{\text{ent}}(t \rightarrow \infty)$ [same as in Eq. (32)], evaluated in a system of size L ; so we will also call it $S_\infty(L)$, ensemble averaged, is plotted as function of L , i.e., how $S_\infty(L)$ scales with L at a various strength of disorder W . No interaction is introduced. One remarkable point is that the plotted curves $S_\infty(L)$ show a non-monotonic evolution as a function of W . For weak W , $S_\infty(L)$ obeys the logarithmic scaling, as we saw in the previous section, while as W approaches the critical value W_c , a sharp distribution of $\langle \hat{n}_k \rangle$ in the crystal momentum space *a la* Eq. (26) tends to be lost, and simultaneously, $S_\infty(L)$ starts to obey the volume-law. In this critical regime, $\langle \hat{n}_k \rangle$ takes values other than 0 or 1, implying an increase in the thermodynamic entropy [cf. Eq. (31)]. Once W exceeds W_c , scaling of $S_\infty(L)$ turns to the area law, as is also the case in a Hermitian localized phase. The evolution of the scaling behavior of $S_\infty(L)$, or $S_\infty(L, W)$ may be summarized as,

$$S_\infty(L) \sim \begin{cases} \log L & (W \ll W_c) \\ L & (W \simeq W_c) \\ 1 & (W > W_c) \end{cases}. \quad (41)$$

Another interesting issue is that the behavior of the

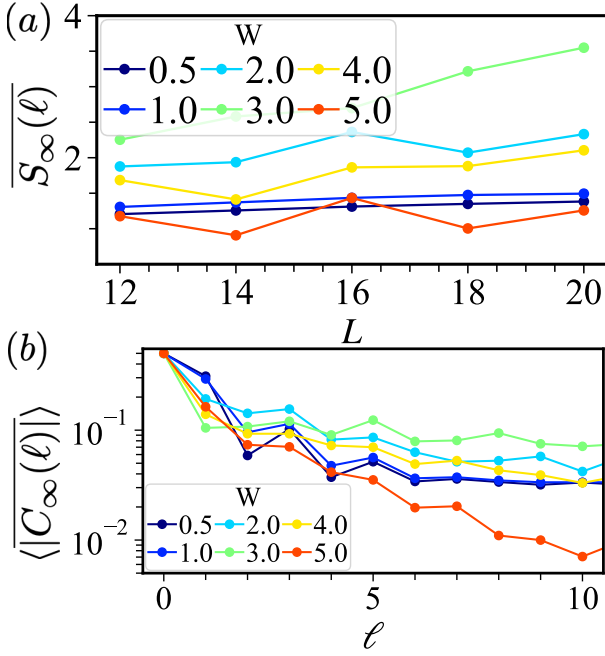


FIG. 9. Size dependence of the entanglement entropy $S_\infty(L)$ (the asymptotic value) [panel (a)] and behavior of the correlation function $C_\infty(l)$ [panel (b)] both in the non-interacting limit. (a) $S_\infty = S_{\text{ent}}(t \rightarrow \infty)$ is calculated in the system of size L and plotted as function of L . Partly, the same data as the ones in Fig. 4 have been replotted. (b) behavior of the correlation function $C_\infty(l) = C_\infty(l, t \rightarrow \infty) = \langle c_j^\dagger c_{j+l} \rangle$, site and sample averaged; as for precise definitions and conditions, see Eqs. (42), (44), and main text. The same wave functions as the ones in Fig. 4 have been used.

correlation function:

$$C_j(l, t) = \langle \psi(t) | c_j^\dagger c_{j+l} | \psi(t) \rangle \quad (42)$$

shows a similar “non-monotonic” dependence on W as then one seen in the entanglement entropy (41). Panel (b) of Fig. 9 shows how this correlation function,

$$C_\infty(l) = \lim_{t \rightarrow \infty} C(l, t) \quad (43)$$

decays with the distance l ; again, in the non-interacting case. To be precise, in the panel the magnitude (absolute value) of the correlation function, both ensemble and site averaged:

$$\langle |C_\infty(l)| \rangle = \left\langle \frac{1}{L} \sum_j |C_j(l, t \rightarrow \infty)| \right\rangle \equiv C_\infty(l) \quad (44)$$

has been plotted. The brackets $\langle \dots \rangle$ represents the ensemble average. At weak W , it is expected to show an algebraic decay:¹¹⁰

$$C_\infty(l) \propto \frac{1 - e^{i\pi l}}{l} \quad (45)$$

reflecting the sharp distribution of $\langle \hat{n}_k \rangle$ in the crystal momentum space (26). As W increases, the decay of

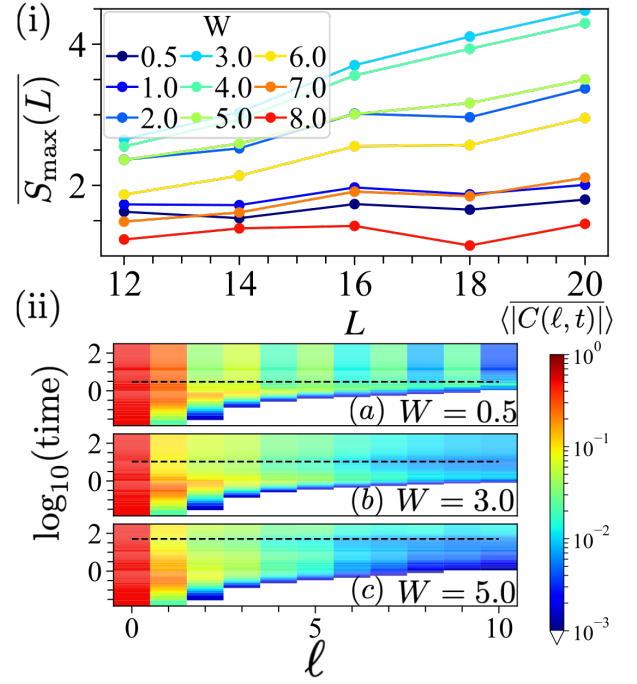


FIG. 10. Scaling of $S_{\text{max}}(L)$ at various strength of disorder W [panel (i)], and behavior of the correlation function $C(l, t)$ in the space time (l, t) [panel (ii)]. (i) $S_{\text{max}}(L)$ [introduced in Eq. (46)] is plotted as a function of L . Partly, the same data as the ones in Fig. 4 have been used. (ii) The behavior of the correlation function $C(l, t)$, introduced in Eq. (42), is shown as a color map for three different values of disorder strength W : (a) $W = 0.5$, (b) $W = 3.0$, and (c) $W = 5.0$ (subpanels). We focused on the magnitude of the correlation function $|C(l, t)|$, which has been also site and ensemble averaged; cf. Eq. (44). The same wave functions as the ones in Fig. 4 have been used.

the correlation function $C_\infty(l)$ becomes slower; compare the greenish plots with the bluish ones, implying that the non-locality of the system is increased. This is in concomitant with the evolution of the scaling of the entanglement entropy $S_\infty(L)$ from logarithmic to volume law; cf. Eq. (41). Once W exceeds W_c , the correlation function $C_\infty(l)$ decreases exponentially, reflecting the localized nature of the wave function.

In the interacting case, we focus on the maximal value of $S_{\text{ent}}(t)$ in its evolution:

$$S_{\text{max}} = \text{Max}[S_{\text{ent}}(t)] \equiv S_{\text{ent}}(t = t_0), \quad (46)$$

instead of $S_\infty = S_{\text{ent}}(t \rightarrow \infty)$ [Eq. (32)]. This is for a practical reason; the Krylov subspace method employed in this work is very effective for reducing the computational difficulty of dealing with a system of large size, while it does not reduce that of a very long-time dynamics.¹¹¹ In Fig. 4, we have already seen an overall behavior of $S_{\text{ent}}(t)$ at different values of W , i.e., both in the delocalized and localized phases, and also at different system sizes L . Here, we have focused on the size-dependence $S_{\text{max}}(L)$ [panel (i) of Fig. 10] in the interact-

ing case. The scaling behavior of $S_{\max}(L)$ at various values of W shows that $S_{\max}(L)$ increases (decreases) with W in the delocalized (localized) regime, indicating that $S_{\max}(L)$ is a good measure of delocalization/localization transition/crossover in this interesting case, playing a similar role as $S_{\infty}(L)$ in the non-interacting case.

We also evaluate the correlation function $C(l, t)$ introduced in Eq. (42) in the interacting case; here, we focus on its time-dependent behavior, since we are interested in how the relaxation of a quantum state $|\Psi(t)\rangle$ due to $\text{Im}(E)$ is reflected in the behavior of the correlation function. Three panels of Fig. 10 (ii) show the time evolution of the correlation function (42) at disorder strength $W = 0.5$ (panel (a)), 3.0 (panel (b)), and 5.0 (panel (c)). The absolute value of the correlation function $|C(l, t)|$ is plotted as a color map in the space of l (the x -axis) and $\log_{10}(\text{time})$ (the y -axis). The black dashed line in each panel represents the time t_0 when $S_{\text{ent}}(t)$ takes the maximal value $S_{\max} = \text{Max}[S_{\text{ent}}(t)]$; see Eq. (46). At weak W [panel (a)], the correlation spreads rapidly; i.e., $C(l, t)$ quickly (i.e., around $t = t_0$) converges to an asymptotic distribution $C_{\infty}(l)$ [see Eq. (43)] which is spatially modulating; reminiscent of the algebraic decay (45) in the non-interacting case; see also Fig. 9 (b), e.g., case of $W = 0.5$ (blue plots). As W is increased, the spreading of correlation becomes delayed; t_0 becomes larger, while the asymptotic distribution $C_{\infty}(l)$ becomes a monotonically decreasing function [case of panels (b) and (c)].

Unlike in the non-interacting case, we have not observed a non-monotonic feature with respect to W in the behavior of the correlation function $C(l, t)$ in the interacting case. Still, we have made a notable observation that t_0 corresponds to the time t when the behavior of the correlation function changes qualitatively; i.e., from a strongly non-equilibrium type behavior ($t < t_0$) to that of a steady state type ($t > t_0$). Once t exceeds t_c , the correlation function $C(l, t)$ tends to become time-independent, indicating that the quantum state $|\Psi(t)\rangle$ reaches a steady state. This observation suggests that S_{\max} is a good quantity that encodes the transition/crossover of the system or of the state $|\Psi(t)\rangle$ from a non-equilibrium to a steady state.

VII. CONCLUDING REMARKS

In this paper, we have highlighted the differences in the dynamical behavior between non-Hermitian and Hermitian disordered systems based on the quasiparticle picture. First, we have systematically studied the dynamical behavior of the many-body HN model, including $n_j(t)$, $n_k(t)$, and S_{ent} , using the Krylov subspace method. Although the difference between non-Hermitian and Hermitian systems are somewhat masked in the behavior of $n_j(t)$ in real space, we find that it sharply manifest in $n_k(t)$, and in S_{ent} as well. In the non-interacting system, we demonstrated both numerically and analytically the characteristic relaxation of $n_k(t)$, where $n_k(t)$ converges

either to 0 (for $k > 0$) or to 1 (for $k < 0$) in the clean limit. This behavior stems from the presence of $\text{Im}(E)$, which is an intrinsic nature of the non-Hermitian system. We also discussed the relationship between the relaxation of $n_k(t)$ and S_{ent} based on the quasiparticle picture and provided an intuitive explanation for the non-monotonic behavior of S_{ent} as a function of W . Interestingly, we found that S_{ent} exhibits a non-monotonic behavior as a function of time in the interacting case. By carefully examining the distribution of $\text{Im}(E)$, especially, through comparison with the non-interacting, we have clarified the nature of this non-monotonic time evolution, which is unique to this non-hermitian interacting system.

The non-monotonic behavior of S_{ent} with respect to time stems from $\text{Im}(E)$, which implies the instability of the many-body localized phase.^{112,113} Recent studies suggest that thermalization symptoms^{114,115} appear even in a strongly disordered system, resulting in the study of many-body delocalization-localization transition^{116–120} at a turning point. They have examined the response of a quantum system to the inclusion of thermal grain¹²¹ and evaluated the imaginary part of eigenenergy,¹²² which may relate to the real-complex transition of the HN model.

For the non-interacting case, we have recently noticed that the non-monotonic behavior of $S_{\text{ent}}(t \rightarrow \infty)$ is also reported in Ref. 110. They have employed a recently proposed numerical approach¹²³ instead of the exact diagonalization and performed calculations in larger system sizes compared to ours. Their findings indicate that the scaling of $S_{\text{ent}}(t \rightarrow \infty)$ exhibits logarithmic-area law transition. This result is contradict with our findings at critical resume ($W \sim W_c$), which may come from the finite size effect. This discrepancy raises a new question: whether S_{ent} obeys volume law scaling in an interacting system. We intend to address this question in future work.

ACKNOWLEDGMENTS

Quspin^{124,125} has been employed for generating the matrix elements of Eq. (1). K.-I.I thanks Marco Schiro and Kohei Kawabata for useful discussions, comments and suggestions. This work was supported by JSPS KAKENHI Grant Numbers JP23KJ0360 (T.O.), JP20K03788 (K.-I.I), and JP21H01005(K.-I.I), and JST SPRING: Grant Number JPMJSP2132 (T.O.).

Appendix A: Notes on the generalized Gibbs ensemble

In the limit of $t \rightarrow \infty$, $t_c(k) < t$ for all k are satisfied, and then $|\Psi(t)\rangle$ reaches an equilibrium state. Generally, we can obtain the corresponding statistical ensemble, assuming principle of maximum entropy under some constraint, such as expectation values of energy or total par-

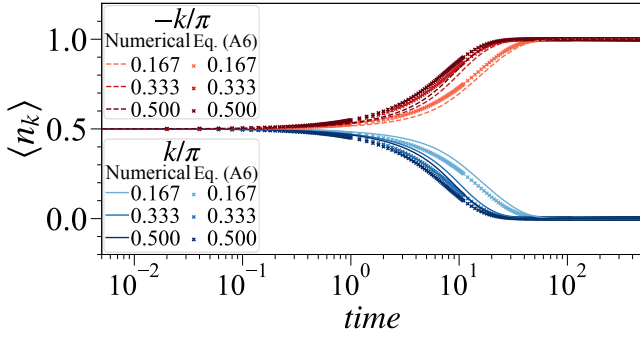


FIG. 11. Time evolution of $\langle \hat{n}_k \rangle$: $L = 12$, $W = 0$, and $V = 0$. The numerical result is obtained by averaging over 100 different initial states (Eq. (B1)). Both solid and dashed line represent numerical result, while a scatter plots represents Eq. (A6).

ticles, using Lagrange multipliers. In case of integrable systems, our target ($W = 0$ and $V = 0$), realized statistical ensemble is called generalized Gibbs ensemble (GGE), which forms maximum entropy under the constraint of \hat{n}_k . GGE is defined as

$$\rho_{GGE} \equiv \frac{e^{-\sum_k \lambda_k \hat{n}_k}}{Z} \quad (A1)$$

where $Z = \text{Tr}[e^{-\sum_k \lambda_k \hat{n}_k}]$, and λ_k is the Lagrange multipliers that imposes constraint $\langle \Psi(t=0) | \hat{n}_k | \Psi(t=0) \rangle = \langle \Psi(\infty) | \hat{n}_k | \Psi(\infty) \rangle$. GGE describes the expectation value of various quantities as well as the saturation value of S_{ent} . The statistical expectation value of \hat{n}_k is defined by

$$\begin{aligned} \langle \hat{n}_k \rangle_{GGE} &\equiv \text{Tr}(\rho_{GGE} \hat{n}_k) \\ &= -\frac{\partial}{\partial \lambda_k} \log(Z) \\ &= \frac{1}{1 + \exp(\lambda_k)} \\ &= \langle \Psi(t) | \hat{n}_k | \Psi(t) \rangle. \end{aligned} \quad (A2)$$

Additionally, the thermodynamic entropy of GGE is in accordance with the saturation value of S_{ent} in the thermodynamic limit, i.e.,

$$\begin{aligned} S_{\text{ent}}(\infty) &= \lim_{L \rightarrow \infty} S_{\text{thermo}} \\ &\equiv \lim_{L \rightarrow \infty} -\text{Tr} \rho_{GGE} \ln \rho_{GGE} \\ &= \lim_{L \rightarrow \infty} \sum s_k \equiv \ell \int dk s(k). \end{aligned} \quad (A3)$$

$S_{\text{ent}}(\infty)$ follows a volume-law ($S_{\text{ent}}(\infty) \propto \ell$) if most $\langle \hat{n}_k \rangle$ take neither 0 or 1, which is consistent to the fact that thermal entropy obeys volume-law.

In the Hermitian case, since \hat{n}_k is a conserved quantity, $\langle \Psi(t) | \hat{n}_k | \Psi(t) \rangle$ remains constant value over time, while $\langle \Psi(t) | \hat{n}_k | \Psi(t) \rangle$ varies during dynamics in the case of the many-body HN model due to the non-unitary time evolution $\partial_t \langle \hat{n}_k \rangle = i \langle \Psi(t) | H^\dagger \hat{n}_k - \hat{n}_k H | \Psi(t) \rangle \neq 0$. Let us focus

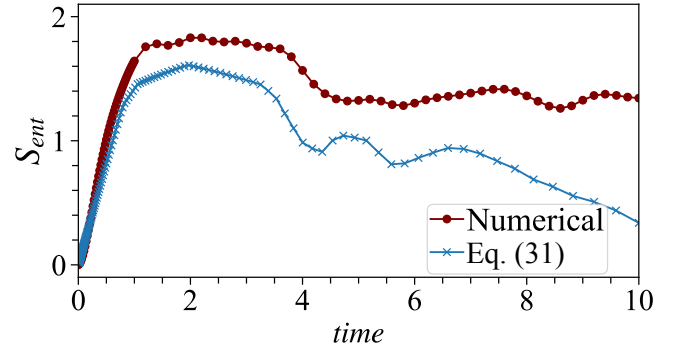


FIG. 12. Time evolution of S_{ent} (red solid line with circles) and the quasiparticle picture (Eq. (31), blue solid line with crosses): $L = 16$, $W = 0$, and $V = 0$. We choose the DW state as the initial state. We take into account the possibility of quasiparticles moving from the left (or right) end to the opposite end in the calculation Eq. (31) (for more details, refer to Ref. 88).

on the relaxation of $\langle \Psi(t) | \hat{n}_k | \Psi(t) \rangle$, which is naively formulated by

$$\begin{aligned} \langle \hat{n}_k \rangle &= \frac{\langle \Psi(0) | e^{iH^\dagger t} \hat{n}_k e^{-iHt} | \Psi(0) \rangle}{\langle \Psi(0) | e^{iH^\dagger t} e^{-iHt} | \Psi(0) \rangle} \\ &= \frac{\text{Tr}(|\Psi_{\{k\}}\rangle^2 \hat{n}_k e^{2\sum_k \text{Im}(\epsilon_k) \hat{n}_k t})}{\text{Tr}(|\Psi_{\{k\}}\rangle^2 e^{2\sum_k \text{Im}(\epsilon_k) \hat{n}_k t})}, \end{aligned} \quad (A4)$$

where ϵ_k is a single particle eigenenergy (see Appendix D) and $\Psi_{\{k\}} = \langle \{n_k\} | \Psi(0) \rangle = \langle n_{k_1} \cdots n_{k_L} | \Psi(0) \rangle$: $|\{n_k\}\rangle$ represents the Fock space in momentum space. Here, we assume $|\Psi_{\{k\}}\rangle^2$ is expressed as a GGE, so that

$$\begin{aligned} \langle \hat{n}_k \rangle &= \frac{\text{Tr}(|\Psi_{\{k\}}\rangle^2 \hat{n}_k e^{2\sum_k \text{Im}(\epsilon_k) \hat{n}_k t})}{\text{Tr}(|\Psi_{\{k\}}\rangle^2 e^{2\sum_k \text{Im}(\epsilon_k) \hat{n}_k t})} \\ &\sim \frac{\text{Tr}(\hat{n}_k e^{\sum_k (-\lambda_k + 2\text{Im}(\epsilon_k)t) \hat{n}_k})}{Z}, \end{aligned} \quad (A5)$$

where $Z = \text{Tr}(e^{\sum_k (-\lambda_k + 2\text{Im}(\epsilon_k)t) \hat{n}_k})$, and we assume superposition consists of various filling to use the knowledge of the grand canonical ensemble. We can derive time dependent behavior of $\langle \hat{n}_k \rangle$, which is defined as

$$\begin{aligned} \langle \hat{n}_k \rangle &= \frac{\text{Tr}(\hat{n}_k e^{\sum_k (-\lambda_k + 2\text{Im}(\epsilon_k)t) \hat{n}_k})}{Z} \\ &= -\frac{\partial}{\partial ((\lambda_k - 2\text{Im}(\epsilon_k)t))} \log(Z) \\ &= \frac{1}{1 + e^{-2\text{Im}(\epsilon_k)t}}, \end{aligned} \quad (A6)$$

where in the last line we take all λ_k to be 0, which is justified in case the initial state is prepared as DW-state. Equation (A6) implies that an imaginary eigenenergy either amplifies or decays a corresponding mode $\langle \hat{n}_k \rangle$ and this relaxation depends on the magnitude of $\text{Im}(\epsilon_k)$.

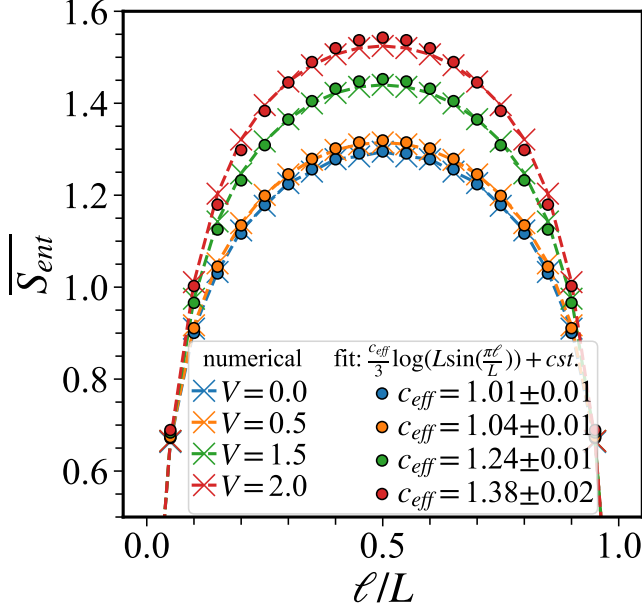


FIG. 13. Scaling of S_{ent} as a function of ℓ/L with various values of V : $L = 20$ and $W = 0$. A dashed line represents a numerical result, while a scatter plot represents a fitting curve.

Appendix B: Time dependence of $\langle \hat{n}_k \rangle$ for free-particle case

In Sec. IV, we observed $\langle \hat{n}_k \rangle$ converge to stationary values more rapidly than Eq. (A6). This discrepancy appears to arise from the fact that we assume $Q = \sum_i k_i$ takes the values ranging from 0 to L to derive an analytical expression of $\langle \hat{n}_k \rangle$, although we employ half-filling sector in actual numerical calculation. To justify Eq. (A6), we select the initial state as

$$|\Psi(0)\rangle = \sum_{Q=0}^{Q=L} \frac{1}{\sqrt{L+1}} |\{n_k^Q\}\rangle, \quad (\text{B1})$$

where $|\{n_k^Q\}\rangle$ is the Fock state that satisfy with $\sum_i k_i = Q$ and we randomly choose the Fock state $|\{n_k^Q\}\rangle$. Figure 11 shows the time evolution of $\langle \hat{n}_k \rangle$ with the initial state given in Eq. (B1). The behavior of $\langle \hat{n}_k \rangle$ is closer to

Eq. (A6) than the result shown in Fig. 5.

Appendix C: Quasiparticle picture for non-reciprocal system

In the HN model, quasiparticles decay or amplify under time evolution, leading to the question of when the quasiparticle picture becomes ill-defined. To address this question, we compare numerical results with the result suggested by the quasiparticle picture, as shown in Fig 12. Initially, the result suggested by the quasiparticle picture agrees with the numerical result; however, as time evolves, it begins to converge to 0, which differs from the numerical result. This discrepancy stems from the assumption within the quasiparticle picture that S_{ent} behaves as thermal entropy, whereas in this case, S_{ent} actually characterizes quantum correlation. Additionally, this discrepancy contrasts with a recent study in which the quasiparticle picture is used to describe the entanglement dynamics in the non-Hermitian system (PT-symmetric system).²⁵ As quasiparticles exhibit unidirectional motion in the HN model, the question of whether the quasiparticle picture quantitatively still describes entanglement dynamics is intriguing. The quasiparticle picture can be compatible and generalized to many physical situations, such as an inhomogeneous initial state¹²⁶ and a state with no quasiparticle pair structure.¹²⁷ Therefore, further study is necessary to generalize the quasiparticle picture to the HN model, which may become a framework for non-Hermitian GGE.

Appendix D: The effect of interaction on the scaling of $S_{\text{ent}}(\infty)$

Figure 13 shows the saturation value of S_{ent} as a function ℓ/L with various values of V . For weak V , a discrepancy between a numerical result (dashed line) and a fitting function (scatter plot), which is a form of Eq. (37), is negligible, but it becomes more noticeable for large V . Although a finite discrepancy exists for large V , a fitting function (Eq. (37)) qualitatively characterizes numerical results, leading us to conclude that the scaling of S_{ent} is logarithmic.

¹ A. Einstein, B. Podolsky, and N. Rosen, Phys. Rev. **47**, 777 (1935).

² S. J. Freedman and J. F. Clauser, Phys. Rev. Lett. **28**, 938 (1972).

³ J.-W. Pan, D. Bouwmeester, H. Weinfurter, and A. Zeilinger, Phys. Rev. Lett. **80**, 3891 (1998).

⁴ A. Aspect, Phys. Rev. D **14**, 1944 (1976).

⁵ A. Aspect, J. Dalibard, and G. Roger, Phys. Rev. Lett. **49**, 1804 (1982).

⁶ A. Aspect, P. Grangier, and G. Roger, Phys. Rev. Lett. **49**, 91 (1982).

⁷ J. M. Deutsch, Phys. Rev. A **43**, 2046 (1991).

⁸ M. Srednicki, Phys. Rev. E **50**, 888 (1994).

⁹ M. Rigol, V. Dunjko, and M. Olshanii, Nature **452**, 854–858 (2008).

¹⁰ M. Rigol, V. Dunjko, V. Yurovsky, and M. Olshanii, Phys. Rev. Lett. **98**, 050405 (2007).

¹¹ M. Rigol, A. Muramatsu, and M. Olshanii, Phys. Rev. A **74**, 053616 (2006).

- ¹² A. Iucci and M. A. Cazalilla, *Phys. Rev. A* **80**, 063619 (2009).
- ¹³ L. Vidmar and M. Rigol, *Journal of Statistical Mechanics: Theory and Experiment* **2016**, 064007 (2016).
- ¹⁴ P. Calabrese and J. Cardy, *Journal of Statistical Mechanics: Theory and Experiment* **2005**, P04010 (2005).
- ¹⁵ V. Alba and P. Calabrese, *Proceedings of the National Academy of Sciences* **114**, 7947 (2017).
- ¹⁶ M. Fagotti and P. Calabrese, *Phys. Rev. A* **78**, 010306 (2008).
- ¹⁷ G. D. Chiara, S. Montangero, P. Calabrese, and R. Fazio, *Journal of Statistical Mechanics: Theory and Experiment* **2006**, P03001 (2006).
- ¹⁸ P. Calabrese, *Physica A: Statistical Mechanics and its Applications* **504**, 31 (2018), lecture Notes of the 14th International Summer School on Fundamental Problems in Statistical Physics.
- ¹⁹ R. Nandkishore and D. A. Huse, *Annual Review of Condensed Matter Physics* **6**, 15 (2015).
- ²⁰ D. A. Abanin, E. Altman, I. Bloch, and M. Serbyn, *Rev. Mod. Phys.* **91**, 021001 (2019).
- ²¹ D. N. Page, *Phys. Rev. Lett.* **71**, 1291 (1993).
- ²² X. Turkeshi and M. Schiró, *Phys. Rev. B* **107**, L020403 (2023).
- ²³ B. Skinner, J. Ruhman, and A. Nahum, *Physical Review X* **9** (2019), 10.1103/physrevx.9.031009.
- ²⁴ Y. Fuji and Y. Ashida, *Phys. Rev. B* **102**, 054302 (2020).
- ²⁵ A. Bácsi and B. Dóra, *Phys. Rev. B* **103**, 085137 (2021).
- ²⁶ Y. L. Gal, X. Turkeshi, and M. Schiró, *SciPost Phys.* **14**, 138 (2023).
- ²⁷ Y. Li, X. Chen, and M. P. A. Fisher, *Phys. Rev. B* **100**, 134306 (2019).
- ²⁸ A. Chan, R. M. Nandkishore, M. Pretko, and G. Smith, *Phys. Rev. B* **99**, 224307 (2019).
- ²⁹ S. Choi, Y. Bao, X.-L. Qi, and E. Altman, *Phys. Rev. Lett.* **125**, 030505 (2020).
- ³⁰ A. Zabalo, M. J. Gullans, J. H. Wilson, S. Gopalakrishnan, D. A. Huse, and J. H. Pixley, *Phys. Rev. B* **101**, 060301 (2020).
- ³¹ X. Turkeshi, R. Fazio, and M. Dalmonte, *Phys. Rev. B* **102**, 014315 (2020).
- ³² S. Sang and T. H. Hsieh, *Phys. Rev. Res.* **3**, 023200 (2021).
- ³³ Z. Yang, D. Mao, and C.-M. Jian, “Entanglement in one-dimensional critical state after measurements,” (2023), arXiv:2301.08255 [quant-ph].
- ³⁴ C. Noel, P. Niroula, D. Zhu, A. Risinger, L. Egan, D. Biswas, M. Cetina, A. V. Gorshkov, M. J. Gullans, D. A. Huse, and C. Monroe, *Nature Physics* **18**, 760 (2022).
- ³⁵ J. M. Koh, S.-N. Sun, M. Motta, and A. J. Minnich, *Nature Physics* (2023), 10.1038/s41567-023-02076-6.
- ³⁶ R. Vasseur, A. C. Potter, Y.-Z. You, and A. W. W. Ludwig, *Phys. Rev. B* **100**, 134203 (2019).
- ³⁷ M. J. Gullans and D. A. Huse, *Phys. Rev. X* **10**, 041020 (2020).
- ³⁸ Y. Kuno, T. Orito, and I. Ichinose, *Phys. Rev. B* **106**, 214304 (2022).
- ³⁹ N. Hatano and D. R. Nelson, *Phys. Rev. B* **56**, 8651 (1997).
- ⁴⁰ N. Hatano and D. R. Nelson, *Phys. Rev. B* **58**, 8384 (1998).
- ⁴¹ N. Hatano and D. R. Nelson, *Phys. Rev. Lett.* **77**, 570 (1996).
- ⁴² S. Longhi, *Phys. Rev. B* **103**, 054203 (2021).
- ⁴³ T. Orito and K.-I. Imura, *Phys. Rev. B* **105**, 024303 (2022).
- ⁴⁴ Y. Saad, *SIAM Journal on Numerical Analysis* **29**, 209 (1992), <https://doi.org/10.1137/0729014>.
- ⁴⁵ S. Aubry and G. André, *Ann. Israel Phys. Soc.* **3**, 133 (1980).
- ⁴⁶ Z. Gong, Y. Ashida, K. Kawabata, K. Takasan, S. Higashikawa, and M. Ueda, *Phys. Rev. X* **8**, 031079 (2018).
- ⁴⁷ S. Yao and Z. Wang, *Phys. Rev. Lett.* **121**, 086803 (2018).
- ⁴⁸ K. Yokomizo and S. Murakami, *Phys. Rev. Lett.* **123**, 066404 (2019).
- ⁴⁹ K.-I. Imura and Y. Takane, *Phys. Rev. B* **100**, 165430 (2019).
- ⁵⁰ K.-I. Imura and Y. Takane, *Progress of Theoretical and Experimental Physics* **2020** (2020), 10.1093/ptep/ptaa100, 12A103, <https://academic.oup.com/ptep/article-pdf/2020/12/12A103/35611802/ptaa100.pdf>.
- ⁵¹ Y. Ashida, Z. Gong, and M. Ueda, *Advances in Physics* **69**, 249 (2020).
- ⁵² T. Yoshida and Y. Hatsugai, *Phys. Rev. B* **106**, 205147 (2022).
- ⁵³ K. Kawabata, K. Shiozaki, and S. Ryu, *Phys. Rev. B* **105**, 165137 (2022).
- ⁵⁴ S.-B. Zhang, M. M. Denner, T. c. v. Bzdušek, M. A. Sentef, and T. Neupert, *Phys. Rev. B* **106**, L121102 (2022).
- ⁵⁵ A. Banerjee, R. Sarkar, S. Dey, and A. Narayan, *Journal of Physics: Condensed Matter* **35**, 333001 (2023).
- ⁵⁶ T. Yoshida and Y. Hatsugai, *Phys. Rev. B* **107**, 075118 (2023).
- ⁵⁷ P. Mognini, O. Arandes, and E. J. Bergholtz, *Phys. Rev. Res.* **5**, 033058 (2023).
- ⁵⁸ R. Qi, J. Cao, and X.-P. Jiang, “Localization and mobility edges in non-hermitian disorder-free lattices,” (2023), arXiv:2306.03807 [cond-mat.dis-nn].
- ⁵⁹ L.-J. Zhai, G.-Y. Huang, and S. Yin, *Phys. Rev. B* **106**, 014204 (2022).
- ⁶⁰ K. Suthar, Y.-C. Wang, Y.-P. Huang, H. H. Jen, and J.-S. You, *Phys. Rev. B* **106**, 064208 (2022).
- ⁶¹ J. Liu and Z. Xu, “From ergodicity to many-body localization in a one-dimensional interacting non-hermitian stark system,” (2023), arXiv:2305.13636 [cond-mat.dis-nn].
- ⁶² L.-J. Zhai, S. Yin, and G.-Y. Huang, *Phys. Rev. B* **102**, 064206 (2020).
- ⁶³ J.-Q. Cheng, S. Yin, and D.-X. Yao, “Dynamical localization transition in the non-hermitian \mathbb{Z}_2 gauge theory,” (2023), arXiv:2307.08750 [cond-mat.dis-nn].
- ⁶⁴ K. Slevin and T. Ohtsuki, *Phys. Rev. Lett.* **82**, 382 (1999).
- ⁶⁵ K. Slevin and T. Ohtsuki, *New Journal of Physics* **16**, 015012 (2014).
- ⁶⁶ K. Kawabata and S. Ryu, *Phys. Rev. Lett.* **126**, 166801 (2021).
- ⁶⁷ X. Luo, T. Ohtsuki, and R. Shindou, *Phys. Rev. B* **104**, 104203 (2021).
- ⁶⁸ S. Heußen, C. D. White, and G. Refael, *Phys. Rev. B* **103**, 064201 (2021).
- ⁶⁹ Inserting a real flux Φ (Hermitian system) changes a localized eigenstate $\psi(j, \Phi = 0) \sim \exp\left(-\frac{|j|}{\xi}\right)$ to $\psi(j, \Phi \neq 0) \sim \exp\left(-\frac{|j|}{\xi} + i\Phi j\right)$. In contrast, inserting an imaginary flux ig (HN-model) modifies a localized eigenstate

$\psi(j, g = 0) \sim \exp\left(-\frac{|j|}{\xi}\right)$ to

$$\begin{aligned} \psi(j, g \neq 0) &\sim \exp\left(-\frac{(1 - g\xi)|j|}{\xi}\right) & \text{if } j < 0 \\ \psi(j, g \neq 0) &\sim \exp\left(-\frac{(1 + g\xi)|j|}{\xi}\right) & \text{if } j \geq 0. \end{aligned}$$

One can easily observe that the delocalization transition is induced by ig and occurs at $g = \xi^{-1}$, from which we can determine the localization length.

⁷⁰ A. Panda and S. Banerjee, Phys. Rev. B **101**, 184201 (2020).

⁷¹ D. C. Brody, Journal of Physics A: Mathematical and Theoretical **47**, 035305 (2013).

⁷² In the Hermitian case, the total probability: $\sum_{\alpha} |c_{\alpha}(t)|^2 (= 1)$ is, of course, conserved. Here, in the non-Hermitian case, the quantity, $\sum_{\alpha} |c_{\alpha}(t)|^2$ itself does not have much meaning, since $\langle \Psi(t) | \Psi(t) \rangle \neq \sum_{\alpha} |c_{\alpha}(t)|^2$. If one expands $\langle \Psi(t) |$ into contributions from different *left* eigenmodes as, $\langle \Psi(t) | = \sum_{\alpha} b_{\alpha}(t) \langle \alpha |$, and uses the biorthogonal relation (8), then one finds, $\langle \Psi(t) | \Psi(t) \rangle = \sum_{\alpha} b_{\alpha}(t) c_{\alpha}(t)$.

⁷³ Later we will encounter the case in which some largest $\text{Im}(E_{\alpha})$'s are quasi-degenerate: $\text{Im}(E_{\alpha_1}) \simeq \text{Im}(E_{\alpha_2}) \simeq \dots$, and contribute equally to $|\Psi(t \rightarrow \infty)\rangle$. Such degeneracy in the imaginary part becomes indeed relevant in the long-time dynamics of the non-interacting case; see Secs. III and VI for details.

⁷⁴ R. Hamazaki, K. Kawabata, and M. Ueda, Phys. Rev. Lett. **123**, 090603 (2019).

⁷⁵ Y. Qin and L. Li, "Pairing-dependent particle separation in non-hermitian fermionic systems," (2023), arXiv:2307.07964 [cond-mat.quant-gas].

⁷⁶ M. Žnidarič, T. c. v. Prosen, and P. Prelovšek, Phys. Rev. B **77**, 064426 (2008).

⁷⁷ J. H. Bardarson, F. Pollmann, and J. E. Moore, Phys. Rev. Lett. **109**, 017202 (2012).

⁷⁸ M. Serbyn, Z. Papić, and D. A. Abanin, Phys. Rev. Lett. **110**, 260601 (2013).

⁷⁹ M. Serbyn, Z. Papić, and D. A. Abanin, Phys. Rev. Lett. **111**, 127201 (2013).

⁸⁰ D. A. Huse, R. Nandkishore, and V. Oganesyan, Phys. Rev. B **90**, 174202 (2014).

⁸¹ D. J. Luitz, N. Laflorencie, and F. Alet, Phys. Rev. B **93**, 060201 (2016).

⁸² E. V. H. Doggen, F. Schindler, K. S. Tikhonov, A. D. Mirlin, T. Neupert, D. G. Polyakov, and I. V. Gornyi, Phys. Rev. B **98**, 174202 (2018).

⁸³ P. P. Mazza, J.-M. Stéphan, E. Canovi, V. Alba, M. Brockmann, and M. Haque, Journal of Statistical Mechanics: Theory and Experiment **2016**, 013104 (2016).

⁸⁴ That is, $\langle \hat{n}_k \rangle$ suggested by GGE (see Appendix A for more details) converges either to 0 or to 1 more slowly than Eq. (30). This discrepancy is because we assume superposition consists of various filling to derive Eq. (A6), whereas in the actual numerical calculation, we consider the half-filling case. If the initial state is prepared as a superposition consists various filling $Q = \sum_i k_i/L$, the time dependence of $\langle \hat{n}_k \rangle$ is akin to Eq. (A6) (see Appendix B).

⁸⁵ A. Avella and F. Mancini, Strongly Correlated Systems: Numerical Methods, Springer Series in Solid-State Sciences (Springer Berlin Heidelberg, 2013).

⁸⁶ Strictly speaking, since we treat a finite system, each quasiparticles can be located in the same subsystem due to the boundary effect (we later comment on this effect), leading to decay in the S_{ent} . Although this effect can be non-negligible in a finite system, it is already known that the less important this effect, the larger the system size we treat;⁸⁸ therefore, we can interpret $t_c(k)$ as a characteristic time scale.

⁸⁷ In numerical calculation, we choose the length of subsystem size ℓ to be small because it may be the simplest way to realize the non-monotonic behavior of S_{ent} . Since $S_{\text{ent}}(t \rightarrow \infty)$ decreases with a decrease of ℓ , in case of small ℓ , the condition $S_{\text{ent}}(t) > S_{\text{ent}}(t \rightarrow \infty)$, which is required to realize such a behavior, becomes easier to achieve.

⁸⁸ R. Modak, V. Alba, and P. Calabrese, Journal of Statistical Mechanics: Theory and Experiment **2020**, 083110 (2020).

⁸⁹ T. Orito and K.-I. Imura, Proceedings of the 29th International Conference on Low Temperature Physics (LT29) (2023), 10.7566/jpscp.38.011187.

⁹⁰ P. Calabrese and J. Cardy, Journal of Physics A: Mathematical and Theoretical **42**, 504005 (2009).

⁹¹ I. Peschel, Journal of Physics A: Mathematical and General **36**, L205 (2003).

⁹² P. Calabrese and J. Cardy, Journal of Statistical Mechanics: Theory and Experiment **2004**, P06002 (2004).

⁹³ C. Holzhey, F. Larsen, and F. Wilczek, Nuclear Physics B **424**, 443 (1994).

⁹⁴ G. Vidal, J. I. Latorre, E. Rico, and A. Kitaev, Phys. Rev. Lett. **90**, 227902 (2003).

⁹⁵ S. Furukawa, V. Pasquier, and J. Shiraishi, Phys. Rev. Lett. **102**, 170602 (2009).

⁹⁶ M. E. Fisher and R. E. Hartwig, Advances in Chemical Physics **15**, 333 (1969).

⁹⁷ B.-Q. Jin and V. E. Korepin, Journal of Statistical Physics **116**, 79 (2004).

⁹⁸ S. Nishimoto, Physical Review B **84** (2011), 10.1103/physrevb.84.195108.

⁹⁹ L. Mao, Y. Hao, and L. Pan, Phys. Rev. A **107**, 043315 (2023).

¹⁰⁰ Y. Ishiguro, J. Sato, and K. Nishinari, "Asymmetry-induced delocalization transition in the integrable non-hermitian spin chain," (2023), arXiv:2101.10647 [cond-mat.stat-mech].

¹⁰¹ K. Yamamoto, M. Nakagawa, M. Tezuka, M. Ueda, and N. Kawakami, Phys. Rev. B **105**, 205125 (2022).

¹⁰² S. R. White, Phys. Rev. Lett. **69**, 2863 (1992).

¹⁰³ U. Schollwöck, Annals of Physics **326**, 96 (2011).

¹⁰⁴ T. Orito, Y. Kuno, and I. Ichinose, Phys. Rev. B **103**, L060301 (2021).

¹⁰⁵ P. Sierant and J. Zakrzewski, Phys. Rev. B **105**, 224203 (2022).

¹⁰⁶ R. Blankenbecler, D. J. Scalapino, and R. L. Sugar, Phys. Rev. D **24**, 2278 (1981).

¹⁰⁷ S. Duane, A. Kennedy, B. J. Pendleton, and D. Roweth, Physics Letters B **195**, 216 (1987).

¹⁰⁸ T. Hayata and A. Yamamoto, Phys. Rev. B **104**, 125102 (2021).

¹⁰⁹ S.-X. Hu, Y. Fu, and Y. Zhang, "Nontrivial worldline winding in non-hermitian quantum systems," (2023), arXiv:2307.01260 [quant-ph].

¹¹⁰ K. Li, Z.-C. Liu, and Y. Xu, "Disorder-induced entanglement phase transitions in non-hermitian systems with

- skin effects,” (2023), arXiv:2305.12342 [quant-ph].
- ¹¹¹ We note that we can also use $S_{\text{ent}}(\infty)$ as a quantity to characterize the delocalization-localization transition. We expect that $S_{\text{ent}}(\infty)$ obeys the volume-law in the delocalized phase and the area-law in the delocalized phase, reflecting the property of $|\alpha_1\rangle$.
- ¹¹² W. De Roeck and F. m. c. Huveneers, Phys. Rev. B **95**, 155129 (2017).
- ¹¹³ T. Thiery, F. m. c. Huveneers, M. Müller, and W. De Roeck, Phys. Rev. Lett. **121**, 140601 (2018).
- ¹¹⁴ M. Kiefer-Emmanouilidis, R. Unanyan, M. Fleischhauer, and J. Sirker, Phys. Rev. Lett. **124**, 243601 (2020).
- ¹¹⁵ F. Evers and S. Bera, “The internal clock of many-body (de-)localization,” (2023), arXiv:2302.11384 [cond-mat.dis-nn].
- ¹¹⁶ N. Macé, F. Alet, and N. Laflorencie, Phys. Rev. Lett. **123**, 180601 (2019).
- ¹¹⁷ N. Laflorencie, G. Lemarié, and N. Macé, Phys. Rev. Res. **2**, 042033 (2020).
- ¹¹⁸ S. Roy and D. E. Logan, Phys. Rev. B **101**, 134202 (2020).
- ¹¹⁹ G. De Tomasi, I. M. Khaymovich, F. Pollmann, and S. Warzel, Phys. Rev. B **104**, 024202 (2021).
- ¹²⁰ M. S. Bahovadinov, W. Buijsman, A. K. Fedorov, V. Gritsev, and D. V. Kurlov, Phys. Rev. B **106**, 224205 (2022).
- ¹²¹ A. Morningstar, D. A. Huse, and J. Z. Imbrie, Phys. Rev. B **102**, 125134 (2020).
- ¹²² A. Morningstar, L. Colmenarez, V. Khemani, D. J. Luitz, and D. A. Huse, Phys. Rev. B **105**, 174205 (2022).
- ¹²³ K. Kawabata, T. Numasawa, and S. Ryu, Phys. Rev. X **13**, 021007 (2023).
- ¹²⁴ P. Weinberg and M. Bukov, SciPost Phys. **2**, 003 (2017).
- ¹²⁵ P. Weinberg and M. Bukov, SciPost Phys. **7**, 20 (2019).
- ¹²⁶ V. Alba, Phys. Rev. B **97**, 245135 (2018).
- ¹²⁷ B. Bertini, E. Tartaglia, and P. Calabrese, Journal of Statistical Mechanics: Theory and Experiment **2018**, 063104 (2018).
- ¹²⁸ D. J. Thouless, Phys. Rev. B **28**, 4272 (1983).

Supplemental Material 1

SINGLE-PARTICLE DYNAMICS IN THE HATANO-NELSON MODEL

In this Supplemental Material, we provide a brief overview of the properties of the Hatano-Nelson model and its single-particle dynamics. The Hatano-Nelson model is a one-dimensional disordered tight-binding system with non-reciprocal hopping,^{39–41} as defined by

$$H = - \sum_{j=0}^{L-1} \left(\Gamma_R |j+1\rangle \langle j| + \Gamma_L |j\rangle \langle j+1| \right) + W_j \sum_{j=0}^{L-1} |j\rangle \langle j|, \quad (\text{D1})$$

where $|j\rangle$ represents a particle located at site j and the notation is the same as Eq. (1) in the main text. The non-Hermiticity of this model is determined by the parameter g in

$$\Gamma_L = e^g \Gamma_0, \quad \Gamma_R = e^{-g} \Gamma_0. \quad (\text{D2})$$

The static properties of this model ($g \neq 0$) are essentially different from the Hermitian case ($g = 0$).

1. Static and dynamical properties (single-particle)

In the Hermitian case: $\Gamma_R = \Gamma_L = \Gamma_0$ (i.e., in the case of symmetric hopping) and under the periodic boundary, the plane waves:

$$|k\rangle = \sum_j e^{ikj} |j\rangle \quad (\text{D3})$$

are eigenstates of the tight-binding model (D1) in the clean limit $W = 0$, and the corresponding eigenenergies are $2\Gamma_0 \cos k$. In the non-Hermitian case: $\Gamma_R \neq \Gamma_L$: under the periodic boundary, the plane waves (D3) are still eigenstates of the Hamiltonian (D1) in the clean limit $W = 0$, but the asymmetry in hopping makes the corresponding eigenenergy ϵ_k complex:

$$\epsilon_k = -2\Gamma_0 (\cosh g \cos k + i \sinh g \sin k). \quad (\text{D4})$$

Under the open boundaries, the eigenstates of Eq. (D1) are no longer the simple sine function composed of the plane waves (D3) even in the clean limit,⁴⁶ but becomes a skin-effect wave function either exponentially damping or amplifying, i.e., the system shows the so-called non-Hermitian skin effect in which the eigen wave functions are localized at the neighborhood of either of the two open boundaries. The corresponding eigenenergies are, on contrary, real. Thus, both under periodic and open boundaries, a specific non-Hermitian feature such as the complex spectrum or the skin effect appears either in the eigenvalues or in the eigen wave functions.

2. Unidirectional motion and effect of disorder

Let us choose, for simplicity, that the initial wave packet $|\psi(0)\rangle$ is localized at a single site: $|\psi(0)\rangle = |j_0\rangle$. Here, we use the notation that $|j\rangle$ represents a real space basis; $|j\rangle$ represents a state localized at site j . At time t this evolves as

$$|\psi(t)\rangle = \sum_k \psi_k e^{-i\epsilon_k t} |k\rangle, \quad (\text{D5})$$

where $\psi_k = \langle k | j_0 \rangle = e^{-ikj_0}$. $|k\rangle$ represents a (crystal) momentum space (k -space) basis or a plane wave eigenstate (D3). Here, we have the clean limit: $W = 0$ in mind. In the more generic case of $W \neq 0$,

$$|\psi(t)\rangle = \sum_n c_n e^{-i\epsilon_n t} |n\rangle, \quad (\text{D6})$$

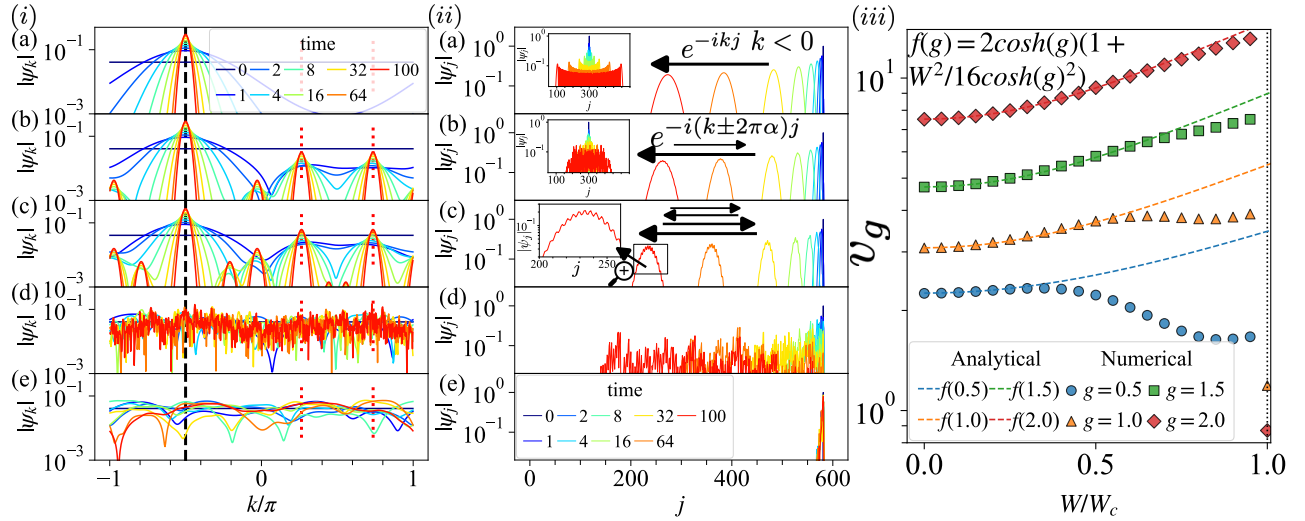


FIG. 14. Time evolution of wave-packets dynamics in the k space: (i-a) $W = 0$; (i-b), $W = 1.0$; (i-c), $W = 5.4$; (i-d), $W = 7.0$; (i-e), $W = 7.0$, in the real space: (ii-a) $W = 0$; (ii-b), $W = 1.0$; (ii-c), $W = 5.4$; (ii-d), $W = 7.0$; (ii-e), $W = 7.0$, for $g = 1.0$ and its velocity: $v_g = \frac{\partial \langle x \rangle}{\partial t}$ as a function of W/W_c , where $W_c = 2 \exp(g)$, for various values g . Black dashed lines in panel (i) represent $k = -\pi/2$, and red dashed lines in panel (i) represent $k = (-\pi/2 \pm 2\pi\alpha) \bmod (2\pi)$. These data are obtained with $j_0 = 581$, $L = 601$ except for the inset panels. The inset panels, including panels (ii-a) and (ii-b), correspond to the Hermitian case with the same disorder strength and different initial state $j_0 = 301$.

where $|n\rangle$ represents the n th single-particle eigenstate of the Hamiltonian (D1) with an eigenenergy ϵ_n ; $H|n\rangle = \epsilon_n|n\rangle$, while $c_n = \langle n|\psi(t=0)\rangle$. Here, $\langle n|$ represents the *left* eigenstate corresponding to the eigenenergy ϵ_n : $\langle n|H = \epsilon_n\langle n|$ and not $|n\rangle^\dagger$; $\langle n| \neq |n\rangle^\dagger$. In Eq. (D5) the initial state $|\psi(0)\rangle$ is expressed as a superposition of plane-wave eigenstates. In the Hermitian case, in the interference of such many plane waves, those satisfying the stationary phase condition survive and contribute to forming the shape of the wave front (see the insets of panels (ii-a) and (ii-b) of Fig. 14). In the non-Hermitian case, on the other hand, the imaginary part of the eigenenergy (D4) plays instead a decisive role in forming the shape of the wave front. In case of $g \neq 0$, the eigenenergy ϵ_n is typically complex, so that the time-evolved wave packet $|\psi(t)\rangle$ literally as given in Eq. (D1) tends to either decay or decay; its norm $\langle \psi(t)|\psi(t)\rangle$ is not conserved due to the contribution from states with $\text{Im} \epsilon_n \neq 0$. In the actual computation, we, therefore, rescale (renormalize) $|\psi(t)\rangle$. We employed the Krylov subspace method with $\delta t = 0.2$ and $M = 15$ (see Eq. (16) in the main text). In the time evolution a plane-wave eigenstate $|k\rangle$ with a maximal imaginary part $\text{Im}(\epsilon_k)$, i.e., $|k = -\pi/2\rangle$ in the superposition (D5). Thus, the initial wave packet $|\psi(0)\rangle$ formed as a superposition of many eigenstate: $|\psi(0)\rangle = \sum_k \psi_k |k\rangle$ tends to evolve into a single eigenstate $|k = -\pi/2\rangle$.

Such an evolution can be indeed seen in the numerical simulation of the density profile $\psi_k(t)$ in the crystal momentum space. Different panels of Fig. 14 show such evolution at different strength of disorder W . In the clean limit: $W = 0$ [panel (i-a)] and at weak disorder; e.g., at $W = 1.0$ [panel (i-b)], one can see that as time evolves contribution from the $k = -\pi/2$ component with a maximal $\text{Im}(\epsilon_k)$ [see Eq. (D4)] tends to become dominant. In case of finite W [panel (i-b) and (i-c)] subdominant peaks associated with the quasi-periodic potential appear. The dominant and subdominant peaks disappear near the localization transition point $W \sim W_c$, and $|\psi_k|$ rapidly oscillates (panel (i-d)). Once a quantum state localizes, initially given momentum distribution almost sustains (panel (i-e)).

As for the specific non-Hermitian characteristics in the real-space dynamics, the remarkable feature is the unidirectional motion of the wave packet, as shown in panel (ii-a) of Fig. 14. By considering the relaxation of ψ_k , we can obtain a trial function defined by

$$|\psi(t)\rangle = \sum_j |j\rangle \frac{\exp\left(-\frac{(j+2 \cosh(g)t)^2}{4 \sinh(g)t}\right)}{(2\pi \sinh(g)t)^{\frac{1}{4}}}. \quad (\text{D7})$$

where $2 \cosh(g) = \text{Re}(\frac{\partial \epsilon_k}{\partial k})|_{k=-\pi/2}$, $2 \sinh(g) = \text{Im}(\epsilon_k)|_{k=-\pi/2}$, and $j_0 = 0$ (see Supplemental Material 2 and Ref. 43). Once the quasi-periodic potential is introduced, the wave packet exhibits a weak modulation, reflecting the subdominant peak of ψ_k (panel (ii-b)). As W increases, this modulation develops into a more complex structure, reflecting the higher-order perturbation process (panel (ii-c)). Near the localization-delocalization transition point $W \sim W_c$, a wave packet exhibits cascade-like spreading (panel (ii-d)). Once W exceeds the W_c , the quantum state localizes

(panel (ii-e)). As observed, the wave packet spreading in the HN model is immune to disorder potential. On the contrary, the velocity of wave packet $v_g = \frac{\partial \langle x \rangle}{\partial t}$ increases as W increases, indicating that disorder enhances wave packet spreading. Through the utilization of the second-order perturbation theory, we can elucidate this peculiar behavior (see Supplemental Material 2). Panel (c) of Fig. 14 shows v_g as a function of W/W_c with various values of g . For large g , analytical (perturbative) results exhibit good agreement with numerical results.

Supplemental Material 2

PERTURBATIVE EFFECT ON NON-RECIPROCAL WAVE-PACKET DYNAMICS

In Supplemental Material 1, we have examined the single particle dynamics of the HN model, where a wave packet exhibits unidirectional motion, and the velocity of unidirectional motion (sliding velocity) increases as W increases for large g . To understand this peculiar behavior, we investigate the effect of the disorder using perturbation theory, considering the quasi-periodic potential as a perturbation term to free-particle dynamics. Before discussing the effect of disorder, we initially provide an intuitive reason why the wave packet exhibits a unidirectional motion in the clean limit. An essential factor is the role of $\text{Im}(E)$, which can either amplify or decay the corresponding eigenstate (plane wave) during dynamics. Consequently, as time passes, the quantum state converges to the eigenstate whose $\text{Im}(E)$ is the maximal. In the presence case, $\text{Im}(E)$ becomes maximal at $k = -\frac{\pi}{2}$. In our previous study,⁴³ we derived the trial function, which captures the unidirectional motion of the wave packet, as given by

$$\begin{aligned}
|\psi(t)\rangle &= \sum_j |j\rangle \int_0^{2\pi} dk \frac{1}{\sqrt{2\pi}} e^{2i \cos(k-ig)t + ikj} \\
&\simeq \sum_j |j\rangle \int_{-\frac{\pi}{2}-\delta k}^{-\frac{\pi}{2}+\delta k} dk \frac{1}{\sqrt{2\pi}} e^{2i \cosh(g)(k+\frac{\pi}{2})t} \times e^{2 \sinh(g)(1-\frac{1}{2}(k+\frac{\pi}{2})^2)t + i(k+\frac{\pi}{2})j} \\
&\simeq \sum_j |j\rangle \int_{-\infty}^{\infty} dk \frac{1}{\sqrt{2\pi}} e^{2i \cosh(g)kt} \times e^{2 \sinh(g)(1-\frac{k^2}{2})t + ikj} \\
&= \sum_j |j\rangle \exp\left(-\frac{(j+2 \cosh(g)t)^2}{4 \sinh(g)t}\right) \times e^{2 \sinh(g)t} / \sqrt{4 \sinh(g)t}.
\end{aligned} \tag{D8}$$

Here, we impose the normalization condition on $|\Psi(t)\rangle$ as

$$|\psi(t)\rangle = \sum_j |j\rangle \frac{\exp\left(-\frac{(j+2 \cosh(g)t)^2}{4 \sinh(g)t}\right)}{(2\pi \sinh(g)t)^{\frac{1}{4}}}. \tag{D9}$$

Using these definitions, we obtained analytical expressions of the sliding velocity $v_g = \frac{\partial \langle x \rangle}{\partial t}$ and mean square displacement $\sigma = \langle x^2 \rangle - \langle x \rangle^2$. Next, we introduce the quasi-periodic disorder and employ a second-order perturbation theory. Since the eigenstates are plane waves, we transform the quasi-periodic potential into momentum space and obtain the perturbation terms given by

$$\sum_{j,k,k'} |k\rangle \langle k| W \cos(2\pi\alpha j) |j\rangle \langle j| |k'\rangle \langle k'| = \sum_{k,\beta=\pm 2\pi\alpha} \frac{W}{2} |k\rangle \langle k+\beta| + h.c. \tag{D10}$$

In this calculation, we approximate the irrational number α as the rational number.^{42,128} Indeed, α is defined as the limit of the ratio of consecutive Fibonacci numbers: $\alpha = \lim_{n \rightarrow \infty} \frac{f_n}{f_{n+1}}$, where $f_{n+1} = f_n + f_{n-1}$ and $f_0 = f_1 = 1$. We obtain perturbation energy and states as follows:

$$\begin{aligned}
E_n^1 &= \langle \psi_n^0 | \left(\sum_{k,\beta=\pm 2\pi\alpha} \frac{W}{2} |k\rangle \langle k+\beta| + h.c. \right) | \psi_n^0 \rangle = 0, \\
|\psi_n^1\rangle &= \frac{W}{2} \left(\frac{|\psi_{n+2\pi\alpha}^0\rangle}{E_n^0 - E_{n+2\pi\alpha}^0} + \frac{|\psi_{n-2\pi\alpha}^0\rangle}{E_n^0 - E_{n-2\pi\alpha}^0} \right), \\
E_n^2 &= \frac{W^2}{4} \left(\frac{1}{E_n^0 - E_{n+2\pi\alpha}^0} + \frac{1}{E_n^0 - E_{n-2\pi\alpha}^0} \right),
\end{aligned} \tag{D11}$$

where the superscript and subscript represent n -th order of perturbation and eigenstate (or eigenenergy), respectively. For large g , $(E_n - E_{n \pm 2\pi\alpha})^{-1}$ is approximated by

$$\begin{aligned}
(E_n^0 - E_{n \pm 2\pi\alpha}^0)^{-1} &= (2 \cosh(g)(\cos(k_n \pm 2\pi\alpha) - \cos(k_n)) + 2i \sinh(g)(\sin(k_n \pm 2\pi\alpha) - \sin(k_n)))^{-1} \\
&= (-4 \cosh(g) \sin(k_n \pm \pi\alpha) \sin(\pm\pi\alpha) - 4i \sinh(g) \cos(k_n \pm \pi\alpha) \sin(\pm\pi\alpha))^{-1} \\
&= \frac{(-4 \sin(\pm\pi\alpha))^{-1}}{\cosh(g) \sin(k_n \pm \pi\alpha) + i \sinh(g) \cos(k_n \pm \pi\alpha)} \\
&= \frac{-1}{4 \sin(\pi\alpha)} \times \frac{\cosh(g) \sin(k_n \pm \pi\alpha) - i \sinh(g) \cos(k_n \pm \pi\alpha)}{\cosh^2(g) \sin^2(k_n \pm \pi\alpha) + \sinh^2(g) \cos^2(k_n \pm \pi\alpha)} \\
&= -\frac{\cosh(g) \sin(k_n \pm \pi\alpha) - i \sinh(g) \cos(k_n \pm \pi\alpha)}{4 \sin(\pm\pi\alpha)(\cosh^2(g) - \cos^2(k_n \pm \pi\alpha))} \\
&\sim -\frac{\cosh(g) \sin(k_n \pm \pi\alpha) - i \sinh(g) \cos(k_n \pm \pi\alpha)}{4 \sin(\pm\pi\alpha) \cosh^2(g)} \tag{D12}
\end{aligned}$$

and thus n th-eigenenergy becomes

$$E_n \sim E_n^0 + E_n^1 + E_n^2 \sim 2 \cosh(g)(1 + \frac{W^2}{16 \cosh^2(g)}) \cos(k_n) + 2i \sinh(g)(1 - \frac{W^2}{16 \sinh^2(g)}) \sin(k_n) \tag{D13}$$

We note that the left eigenvector is the transpose of the right eigenvector multiplied by a constant factor: $\langle\langle n^L | \propto |n^R\rangle^T \equiv (|\psi_n^0\rangle + |\psi_n^1\rangle)^T$. Additionally, the normalization condition $\langle\langle n^L | n^R \rangle = 1$ is almost satisfied for large g . Using eigenenergies and eigenvectors, we can derive $|\Psi(t)\rangle$, which is given by

$$\begin{aligned}
|\Psi(t)\rangle &= \sum_n e^{-iE_n t} |n^R\rangle \langle\langle n^L | \Psi(0)\rangle\rangle \\
&\sim \sum_n e^{-i(E_n^0 + E_n^2)t} (|\psi_n^0\rangle + \sum_{\beta=\pm 2\pi\alpha} \frac{W}{2(E_n^0 - E_{n+\beta}^0)} |\psi_{n+\beta}^0\rangle) (\langle\langle \psi_n^0 | + \sum_{\beta=\pm 2\pi\alpha} \frac{W}{2(E_n^0 - E_{n+\beta}^0)} \langle\langle \psi_{n+\beta}^0 |) |\Psi(0)\rangle\rangle \\
&= \frac{1}{\sqrt{L}} \sum_{n,j} |j\rangle \langle j| e^{-i(E_n^0 + E_n^2)t} (|\psi_n^0\rangle + \sum_{\beta=\pm 2\pi\alpha} \frac{W}{2(E_n^0 - E_{n+\beta}^0)} |\psi_{n+\beta}^0\rangle) (1 + \sum_{\beta=\pm 2\pi\alpha} \frac{W}{2(E_n^0 - E_{n+\beta}^0)}) \\
&= \frac{1}{L} \sum_{n,j} |j\rangle e^{-i(E_n^0 + E_n^2)t} e^{ik_n j} (1 + \sum_{\beta=\pm 2\pi\alpha} \frac{W}{2(E_n^0 - E_{n+\beta}^0)} e^{ik_\beta j}) (1 + \sum_{\beta=\pm 2\pi\alpha} \frac{W}{2(E_n^0 - E_{n+\beta}^0)}) \\
&= \frac{1}{L} \sum_{n,j} |j\rangle e^{-i(E_n^0 + E_n^2)t} e^{ik_n j} (1 + \sum_{\beta=\pm 2\pi\alpha} \frac{W}{2(E_n^0 - E_{n+\beta}^0)} e^{ik_\beta j} + \sum_{\beta=\pm 2\pi\alpha} \frac{W}{2(E_n^0 - E_{n+\beta}^0)}) + \mathcal{O}(\cosh^{-2}(g)) \\
&\sim \frac{\exp\left(-\frac{(j+2 \cosh(g)(1 + \frac{W^2}{16 \cosh^2(g)})t)^2}{4 \sinh(g)(1 - \frac{W^2}{16 \sinh^2(g)})t}\right)}{(2\pi \sinh(g)(1 - \frac{W^2}{16 \sinh^2(g)})t)^{\frac{1}{4}}} \times (1 + \sum_{\beta=\pm 2\pi\alpha} \frac{W e^{ik_\beta j}}{2(E_n^0 - E_{n+\beta}^0)}|_{k_n=\frac{-\pi}{2}} + \sum_{\beta=\pm 2\pi\alpha} \frac{W}{2(E_n^0 - E_{n+\beta}^0)}|_{k_n=\frac{-\pi}{2}}) \\
&= \frac{\exp\left(-\frac{(j+2 \cosh(g)(1 + \frac{W^2}{16 \cosh^2(g)})t)^2}{4 \sinh(g)(1 - \frac{W^2}{16 \sinh^2(g)})t}\right)}{(2\pi \sinh(g)(1 - \frac{W^2}{16 \sinh^2(g)})t)^{\frac{1}{4}}} \times (1 + i \frac{\sinh(g) \sin(\pi\alpha)(1 + \cos(2\pi\alpha j)) + \cosh(g) \cos(\pi\alpha) \sin(2\pi\alpha j)}{4 \sin(\pi\alpha) \cosh(g)^2}) \tag{D14}
\end{aligned}$$

We can extract a distinctive characteristic of $|\Psi(t)\rangle$ from Eq. (D14). As the second term of Eq. (D14) in the last line consists solely of imaginary numbers, its contribution to $\langle x \rangle$ and $\langle x^2 \rangle$ become $\mathcal{O}(\cosh^{-2}(g))$ and can be considered negligible. Therefore, we can obtain the perturbative solution by adding ϵ_n^2 to ϵ_n^0 . The perturbative effect of the eigenenergy on the wave packet dynamics differs from that of the eigenstate. The perturbative correction in the eigenenergy leads to an increase in v_g as a function of W , while that in the eigenstate is irrelevant for dynamics since non-interference occurs, resulting in unidirectional motion immune to the disorder potential. Once interference becomes non-negligible, a cascade-like spreading emerges.